







Halo mass-observable proxy scaling relations and their dependencies on galaxy and group properties

ZIWEN ZHANG ^{1,2} HUIYUAN WANG ^{1,2} WENTAO LUO ^{1,2} HOUJUN MO ³ JUN ZHANG ^{4,5} XIAOHU YANG,^{4,5}
HAO LI,^{1,2} AND QINXUN LI ^{1,2}

¹*CAS Key Laboratory for Research in Galaxies and Cosmology, Department of Astronomy, University of Science and Technology of China, Hefei, Anhui 230026, China; Email: ziwenzhang@mail.ustc.edu.cn, whywang@ustc.edu.cn*

²*School of Astronomy and Space Science, University of Science and Technology of China, Hefei 230026, China*

³*Department of Astronomy, University of Massachusetts, Amherst, MA 01003-9305, USA*

⁴*Department of Astronomy, Shanghai Jiao Tong University, Shanghai 200240, China*

⁵*Shanghai Key Laboratory for Particle Physics and Cosmology, Shanghai 200240, China*

ABSTRACT

Based on the DECaLS shear catalog, we study the scaling relations between halo mass (M_h) and various proxies for SDSS central galaxies, including stellar mass (M_*), stellar velocity dispersion (σ_*), abundance matching halo mass (M_{AM}) and satellite velocity dispersion (σ_s), and their dependencies on galaxy and group properties. In general, these proxies all have strong positive correlations with M_h , consistent with previous studies. We find that the M_h - M_* and M_h - σ_* relations depend strongly on group richness (N_{sat}), while the M_h - M_{AM} and M_h - σ_s relations are independent of it. Moreover, the dependence on star formation rate (SFR) is rather weak in the M_h - σ_* and M_h - σ_s relations, but very prominent in the other two. σ_s is thus the best proxy among them, and its scaling relation is in good agreement with hydro-dynamical simulations. However, estimating σ_s accurately for individual groups/clusters is challenging because of interlopers and the requirement for sufficient satellites. We construct new proxies by combining M_* , σ_* , and M_{AM} , and find the proxy with 30% contribution from M_{AM} and 70% from σ_* can minimize the dependence on N_{sat} and SFR. We obtain the M_h -supermassive black hole (SMBH) mass relation via the SMBH scaling relation and find indications for rapid and linear growth phases for SMBH. We also find that correlations among M_h , M_* and σ_* change with M_* , indicating that different processes drive the growth of galaxies and SMBH at different stages.

Keywords: gravitational lensing - galaxies: halos

1. INTRODUCTION

In the standard Λ CDM paradigm, dark matter halos, approximately in dynamical equilibrium, form hierarchically through gravitational instability. Galaxies form and evolve in the potential wells of dark matter halos (e.g. White & Rees 1978; Fall & Efstathiou 1980; Mo et al. 2010). Galaxies residing in one halo are regarded as a galaxy group or a cluster. In recent years, many studies have concentrated on establishing galaxy - halo connections, manifested as scaling relations between halo mass and galaxy and group properties (proxies). These scaling relations can be used to estimate the halo mass of galaxy groups and clusters (Yang et al. 2005; Zahid et al. 2016; Seo et al. 2020), constrain cosmology (Bocquet et al. 2015; Caldwell et al. 2016), and study galaxy formation models (see Mo et al. 2010; Wechsler & Tinker 2018; Chen et al. 2021a,b, for references).

In these scaling relations, halo mass (M_h) is not a direct observable. M_h estimation usually requires high-quality data and/or sophisticated techniques, and sometimes model assumptions. Numerous studies have developed various methods to constrain the halo mass, including the virial mass estimator (e.g. Carlberg et al. 2001; Rines et al. 2013; Abdullah et al. 2020), X-ray emission (Ruel et al. 2014), Sunyaev-Zel'dovich (SZ) effects (Ruel et al. 2014; Rines et al. 2016), caustics technique (e.g. Rines & Diaferio 2006; Rines et al. 2013), abundance matching (Yang et al. 2007) and weak lensing (e.g. Mandelbaum et al. 2006, 2016; Hoekstra 2007; Leauthaud et al. 2012; Velander et al. 2014; Gonzalez et al. 2015; Han et al. 2015; Hudson et al. 2015; Viola et al. 2015; Luo et al. 2018; Gonzalez et al. 2021; Rana et al. 2022; Zhang et al. 2021, 2022b). Various halo mass proxies have been investigated, such as stellar mass, group rich-

ness, stellar velocity dispersion, group total stellar mass or luminosity, and satellite velocity dispersion.

Among these studies, the most widely discussed halo mass proxy is the stellar mass (M_*) of central galaxies. And the corresponding scaling relation is referred to as stellar mass-halo mass relation (hereafter SHMR) (e.g. Yang et al. 2003; Moster et al. 2010; Leauthaud et al. 2012; Li et al. 2013; Mandelbaum et al. 2016; Kravtsov et al. 2018; Wechsler & Tinker 2018; Behroozi et al. 2019; Zhang et al. 2021, 2022b). The SHMR can be used to constrain galaxy formation processes. For example, $M_*/M_h/(\Omega_b/\Omega_m)$ is usually regarded as the baryon-to-star conversion efficiency. The mean efficiency peaks around the Milky-way like galaxies, with a value of about 20%, and declines quickly toward both lower and higher M_* ends. At lower M_* , the efficiency is believed to be suppressed by supernova feedback and stellar winds (e.g. Dekel & Silk 1986; Kauffmann & Charlot 1998; Cole et al. 2000; Hopkins et al. 2012), while the feedback from active galactic nuclei (AGN) is suggested to be responsible for suppressing the efficiency at higher M_* (e.g. Silk & Rees 1998; Croton et al. 2006; Fabian 2012; Heckman & Best 2014; Cui et al. 2021). The SHMR has large scatter, which depends on galaxy properties, such as color, star formation rate and morphology (e.g. More et al. 2011; Rodríguez-Puebla et al. 2015; Mandelbaum et al. 2016; Behroozi et al. 2019; Lange et al. 2019a; Romeo et al. 2020; Zhang et al. 2021; Bilicki et al. 2021; Posti & Fall 2021; Xu & Jing 2022; Wang et al. 2023a). Research based on simulations suggests that the dependence is related to both halo assembly and AGN feedback (Cui et al. 2021). More recently, several studies found a number of massive star-forming/spiral galaxies that exhibit very high star formation efficiency, about 50%-60% (e.g. Posti et al. 2019; Zhang et al. 2022b). Their results indicate that these galaxies can convert most of their halo gas into stars, implying that AGN feedback is inefficient in them. The scatter of SHMR depends also strongly on satellite properties (Lu et al. 2016; Zhou & Han 2022). All these results suggest that the SHMR and its scatter contain valuable information about galaxy formation and halo assembly.

Stellar velocity dispersion (σ_*) directly reflects the gravitational potential of the galaxy, and is well correlated with the stellar mass. Given the SHMR, one may expect a strong correlation between stellar velocity dispersion and halo mass. The σ_* measurement is straightforward, and its systematic uncertainty may be lower than the stellar mass, making the stellar velocity dispersion an ideal alternative to stellar mass as a halo-mass proxy. Previous studies on this connection find

that the stellar velocity dispersion is indeed a robust proxy for halo mass (e.g. Zahid et al. 2016, 2018; Seo et al. 2020; Sohn et al. 2020). The M_h - σ_* relation also has other important applications. For instance, Shankar et al. (2020) found that the M_h - σ_* relation and the large-scale clustering of AGNs can be used to constrain the shape and amplitude of the scaling relation between supermassive black hole (SMBH) mass and galaxy properties, as well as to constrain the radiative efficiency of AGNs. The halo masses in these observational studies are estimated via abundance matching and satellite kinematics. It is required to have a weak lensing based investigation as an independent check. Moreover, it is also interesting to investigate if the SHMR and M_h - σ_* relation are independent of each other. Studying the bivariate correlation may be particularly important for understanding the connection between AGN feedback, galaxy growth and halo environments.

Previous studies have also adopted the total stellar mass or total luminosity of group members as a halo mass proxy, and found good correlations with halo mass (e.g. Yang et al. 2005; Conroy et al. 2007; Han et al. 2015). Han et al. (2015) performed a maximum-likelihood weak-lensing analysis and found that the group luminosity has the tightest relation with weak lensing halo mass among all single proxies they investigated. The group luminosity and stellar mass have been used to estimate the halo mass based on abundance matching (e.g. Yang et al. 2005, 2007). The inferred halo mass is referred to as the abundance matching halo mass, denoted by M_{AM} , in the following. Luo et al. (2018) and Gonzalez et al. (2021) studied the relation between M_{AM} and halo mass based on weak lensing. Gonzalez et al. (2021) further investigated the dependence of the M_h - M_{AM} relation on galaxy morphology and found that the relation for early-type centrals is closer to the one-to-one relation than the relation based on all types of centrals.

Satellite kinematics, which results from the equilibrium of a gravitational system, can also provide a measurement of halo mass. Many investigations have been carried out to study the relation between satellite velocity dispersion (σ_s) and halo mass using both simulations (e.g. Evrard et al. 2008; Li et al. 2012; Munari et al. 2013; Saro et al. 2013) and observational data (e.g. Rines & Diaferio 2006; Yang et al. 2007; Hoekstra 2007; Rines et al. 2013; Ruel et al. 2014; Gonzalez et al. 2015; Han et al. 2015; Viola et al. 2015; Rines et al. 2016; Abdullah et al. 2020; Gonzalez et al. 2021; Rana et al. 2022). Evrard et al. (2008) used dark matter particles to calculate σ_s and found that the relation has small scatter. Munari et al. (2013) and Saro et al. (2013) found a weak

bias (less than 10%) when using simulated subhalos or satellite galaxies to derive σ_s . They all found that halo mass is roughly proportional to σ_s^3 , consistent with theoretical expectations.

Observationally, various methods have been applied to establish the M_h - σ_s relation. For example, some studies estimated the halo mass based on the caustics technique (e.g. Rines & Diaferio 2006; Rines et al. 2013), SZ effect (e.g. Ruel et al. 2014; Rines et al. 2016) and X-ray observation (Ruel et al. 2014). These studies usually focused on individual galaxy clusters and the obtained relations are broadly consistent with those from simulations. However, the results based on weak lensing data appear complex. Some studies obtained similar slopes but different amplitudes in comparison to relations obtained from simulations (e.g. Gonzalez et al. 2021; Zhang et al. 2022b), and some obtained even different slopes (e.g. Han et al. 2015; Gonzalez et al. 2015; Viola et al. 2015; Rana et al. 2022). Hoekstra (2007) obtained the relation for massive clusters and found it in agreement with simulations but with larger scatter. In addition, very few studies extended the M_h - σ_s relation to $M_h < 10^{13} M_\odot$ (e.g. Han et al. 2015; Zhang et al. 2022b).

The main goal of this paper is to study various halo mass proxies (stellar mass M_* , stellar velocity dispersion σ_* , abundance matching halo mass M_{AM} , satellite velocity dispersion σ_s , and combinations of them) and their relations with the halo mass obtained from weak lensing. We also investigate their dependencies on other galaxy/group properties to shed light on underlying physical processes, and evaluate the performance of these halo mass proxies. The outline of this paper is as follows. In Section 2, we describe sample selections and the weak lensing shear catalog to be used. Section 3 presents measurements of weak lensing and satellite kinematics. We also introduce in this section a proxy based on combinations of parameters and the way to evaluate the performance of halo mass proxies. In Section 4, we show the scaling relations we obtain and their dependencies on other galaxy and group properties. Finally, we summarize our results in Section 5. Throughout this paper, we assume a flat Λ CDM cosmology with $\Omega_m = 0.307$, $\Omega_b = 0.048$, $\Omega_\Lambda = 0.693$ and $h = 0.678$. Here, $h = H_0/100 \text{ km s}^{-1} \text{ Mpc}^{-1}$ and H_0 is the Hubble constant (Planck Collaboration et al. 2016).

2. OBSERVATIONAL DATA

2.1. Central galaxy samples

The galaxies used in this paper are drawn from the New York University Value Added Galaxy Catalog

(NYU-VAGC¹ Blanton et al. 2005) of the Sloan Digital Sky Survey Data Release 7 (SDSS DR7) (Abazajian et al. 2009). We select galaxies with r -band Petrosian magnitude $r \leq 17.72$, with redshift in the range of $0.01 \leq z \leq 0.2$ and with redshift completeness $C_z > 0.7$. We use the group catalog² of Yang et al. (2005, 2007) to classify central and satellite galaxies. Central galaxies are defined as the most massive galaxies in galaxy groups. As shown in the next section, we obtain the halo mass by using the Dark Energy Camera Legacy Survey (DECaLS, Dey et al. 2019). About 32% of SDSS DR7 galaxies do not overlap with the DECaLS. This leaves a sample of 323,448 central galaxies.

M_* of the central galaxies are obtained by cross-matching with the MPA-JHU DR7 catalog³ (Kauffmann et al. 2003; Brinchmann et al. 2004). They are calculated by fitting the SDSS $ugriz$ photometry to models of galaxy spectral energy distribution. σ_* is provided by NYU-VAGC. M_{AM} for each central galaxy is provided by the group catalog (Yang et al. 2007). Here, we mainly use M_{AM} based on the group total stellar mass. The estimate of σ_s will be described in Section 3.2 and the combined proxies are introduced in Section 3.3.

Not all galaxies have valid estimations of M_* , σ_* , star-formation rate (SFR) and M_{AM} . For example, a small fraction of galaxies have no measurement of σ_* (usually low mass galaxies), and some have unreasonably high σ_* (e.g. $\sigma_* \sim 1000 \text{ km s}^{-1}$). Moreover, a fraction of low mass galaxies have no available M_{AM} because M_{AM} can only be estimated in a complete sample. We thus construct two total samples. The first one, referred to as ATotal, has measurements of M_* and SFR and $0 < \sigma_*/\text{km s}^{-1} < 630$ of 299,806 galaxies. This sample is used to study the M_h - M_* and M_h - σ_* relations (Section 4.1 and 4.2). The second one, referred to as BTotal, requires measurements of M_{AM} in addition. This requirement removes 60,769 galaxies. The BTotal sample is used to study the M_h - M_{AM} relation (Section 4.3). When we study the M_h - σ_s relation (Section 4.4), both samples are used. We do not use BTotal sample to study the M_h - M_* and M_h - σ_* relations, because this sample excludes many low-mass galaxies. We list the sample selection, the sample size and the sections where the samples are used in Table 1.

We will also consider the dependencies of the various relations mentioned above on several galaxy properties, such as M_* , σ_* and SFR, and one group prop-

¹ <http://sdss.physics.nyu.edu/vagc/>

² <https://gax.sjtu.edu.cn/data/Group.html>

³ <https://wwwmpa.mpa-garching.mpg.de/SDSS/DR7/>

erty, the group richness. The galaxy SFR is obtained by cross-matching with the MPA-JHU DR7 catalog, where the SFRs of individual galaxies were derived from spectroscopic and photometric data of the SDSS. We adopt the demarcation line proposed by Bluck et al. (2016), to separate star-forming and quenched galaxies. Thus, the ATotal (BTotal) sample is divided into ASF (BSF) and AQ (BQ) subsamples, corresponding to star-forming and quenched galaxies, respectively. For each central galaxy, its group richness is quantified in terms of the number of satellites (hereafter N_{sat}) provided by the group catalog. We divide the ATotal (BTotal) sample into four subsamples, AC0, AC1, AC2 and AC3 (BC0, BC1, BC2 and BC3), where AC0 and BC0 have $N_{\text{sat}} = 0$, AC1 and BC1 have $N_{\text{sat}} \geq 1$, AC2 and BC2 have $1 \leq N_{\text{sat}} \leq 2$, and AC3 and BC3 have $N_{\text{sat}} \geq 3$. These subsamples are also listed in Table 1. These samples are sometimes referred to as the A-series and B-series samples, respectively.

2.2. DECaLS shear catalog

We use the shear catalog based on the DECaLS DR8 imaging data (Dey et al. 2019; Zou et al. 2019) to measure galaxy-galaxy lensing signals. Galaxy shapes are measured by using the FOURIER_QUAD pipeline which measures galaxy shear with great accuracy even for extremely faint images (signal-to-noise ratio < 10). The pipeline was tested both with simulations (Zhang et al. 2015) and with observations (See Zhang et al. (2019) for the CFHTLenS data and Wang et al. (2021); Zhang et al. (2022a) for the DECaLS data). The shear catalog covers more than ten thousand square degrees in the g , r , and z bands, with 99, 111 and 116 million distinct galaxies, respectively. The FOURIER_QUAD method counts images of the same galaxy but in different exposures as different images.

A machine learning algorithm based on decision trees is implemented to calculate photometric redshifts of galaxies in the shear catalog (Zhou et al. 2021). Eight parameters, including the r -band magnitude, $(g - r)$, $(r - z)$, $(z - W1)$, and $(W1 - W2)$ colors, half-light radius, axial ratio, and shape probability, are adopted in the training progress. The photo- z error of each individual shear image is obtained by perturbing the photometry of the galaxy. The procedures are as follows: (i) the uncertainty was assumed to follow a Gaussian distribution with the standard deviation equal to the photometric error; (ii) a random value generated from the distribution was added to the observed flux in each band to obtain a ‘‘perturbed’’ flux; (iii) the perturbation was repeated multiple times, and the standard deviation of the photo- z estimates from the perturbations was used

as the error of the photo- z (see details in Zhou et al. 2021).

3. METHODS OF ANALYSIS

In this section, we describe the methods to measure halo mass and satellite kinematics from observational data. In addition, we present our methods for constructing combined halo mass proxies and for evaluating the performance of these proxies.

3.1. Weak lensing measurements

We measure the excess surface density (ESD) by using the r - and z -band data of the DECaLS shear catalog. Zhang et al. (2017) proposed a probability distribution function (PDF) symmetrization method to minimize the statistical uncertainty in shear signal. We apply a modified version of this method and estimate the ESD in physical coordinates by

$$\Delta\Sigma(R) = \gamma_t(R)\Sigma_{\text{crit}}. \quad (1)$$

The details and general discussion about different sources of systematic errors of the PDF-symmetrization method in measuring the ESD signal are given in a companion paper (Wang et al. 2022). Error bars of ESD signals are estimated by using 150 bootstrap samples (Barrow et al. 1984).

To model the ESD signal, we follow previous studies (e.g. Mandelbaum et al. 2008; Leauthaud et al. 2010; Luo et al. 2018; Zhang et al. 2022b) and apply a halo model consisting of three terms:

$$\Delta\Sigma = \Delta\Sigma_{\text{stellar}} + \Delta\Sigma_{\text{NFW}} + \Delta\Sigma_{2\text{h}}. \quad (2)$$

The first term is the stellar mass term that represents the contribution from the galaxy stellar mass. We treat the galaxy as a point mass and adopt the average stellar mass of the galaxy sample directly from the observation. The second term is the one-halo term, which is the contribution from the host dark matter halo, and we assume the halo to follow the Navarro–Frenk–White (NFW; Navarro et al. 1997) density profile. The NFW profile has two free parameters: the dark halo mass (m_{h}) and the halo concentration (c). The dark halo mass m_{h} is defined as the total dark matter mass within a spherical region of radius $r_{200\text{m}}$. Inside this region, the mean mass density is equal to 200 times the mean matter density of the Universe. We use the central galaxy as the tracer of the halo center. We adopt the equations from Yang et al. (2006) to analytically calculate the one-halo term. In the modeling process, we ignore the off-center effect (Mandelbaum et al. 2016), which has been shown to be a minor factor in halo mass estimation

Table 1. Sample selection used in our analysis

Sample ^(a)	Sample criteria ^(b)	subsample criteria ^(c)	Sample Size	Section ^(d)
ATotal	$0 < \sigma_* < 630$		299,806	3.2, 4.1, 4.2, 4.4
AC0	available M_*	$N_{\text{sat}} = 0$	262,404	3.2, 4.1, 4.2
AC1	available SFR	$N_{\text{sat}} \geq 1$	37,402	3.2, 4.1, 4.4
AC2		$1 \leq N_{\text{sat}} \leq 2$	30,245	3.2, 4.1, 4.2
AC3		$N_{\text{sat}} \geq 3$	7,157	3.2, 4.1, 4.2
ASF		star-forming	176,202	4.1, 4.2
AQ		quenched	123,604	4.1, 4.2
BTotal	$0 < \sigma_* < 630$		239,037	4.3, 4.5
BC0	available M_*	$N_{\text{sat}} = 0$	204,514	4.3, 4.5
BC1	available SFR	$N_{\text{sat}} \geq 1$	34,523	4.4
BC2	available M_{AM}	$1 \leq N_{\text{sat}} \leq 2$	27,477	4.3, 4.4
BC3		$N_{\text{sat}} \geq 3$	7,046	4.3, 4.4, 4.5
BSF		star-forming	123,796	4.3, 4.4, 4.5
BQ		quenched	115,241	4.3, 4.4, 4.5

^(a) ATotal and BTotal are two total samples, and the rest are corresponding subsamples.

^(b) The selection criteria is applied to the corresponding total samples and subsamples.

^(c) The selection criterion is only applied to the corresponding subsample.

^(d) The sections where the samples are used.

(Wang et al. 2022). The third term is the two-halo term, which represents the contribution from other halos. To calculate this term, we project the halo-matter cross-correlation function, ξ_{hm} , along the line-of-sight. Here, $\xi_{\text{hm}} = b(m_{\text{h}})\xi_{\text{mm}}$, with $b(m_{\text{h}})$ being the halo bias (e.g. Mo & White 1996; Tinker et al. 2010) and ξ_{mm} being the linear matter-matter correlation function. We use *COLOSSUS* (Diemer 2018) to model both $b(m_{\text{h}})$ and ξ_{mm} .

There are two free parameters (m_{h} and c) in our model. The priors of these parameters are set to be flat, with m_{h} in the range of [10.0, 16.0] in logarithmic space and c in the range of [1.0, 16.0]. To constrain them, we use *emcee* (Foreman-Mackey et al. 2013) to run a Monte Carlo Markov Chain (MCMC). In the following, the results shown are the median values of the posteriors, and the error bars correspond to the 16 and 84 percent of the posterior distribution (See Luo et al. (2018) for more details on the modeling and fitting process). Since we include the stellar mass term in our model, m_{h} only accounts for cold dark matter, diffuse gas, and satellites around centrals. Thus, throughout this paper, we use the total mass $M_{\text{h}} = m_{\text{h}} + M_*$ instead of m_{h} to represent the halo mass.

3.2. Satellite kinematics

Satellite kinematics can also serve as a powerful probe of dark matter halos (e.g. McKay et al. 2002; van den Bosch et al. 2004; More et al. 2011; Wojtak & Mamon 2013; Lange et al. 2019b; Abdullah et al. 2020; Seo et al. 2020). One major concern in satellite kinematics studies is the contamination of interlopers (see e.g. van den

Bosch et al. 2004; Mamon et al. 2010). Recently, Zhang et al. (2022b) used weak lensing technique to estimate the halo masses of their central galaxy samples and derived the corresponding halo virial radius, $r_{200\text{m}}$, and halo virial velocity, $v_{200\text{m}}$. They selected satellite candidates from a reference galaxy sample using the following set of criteria: $r_{\text{p}} \leq r_{200\text{m}}$, $|\Delta v| \leq 3v_{200\text{m}}$, and $M_{\text{s}} < M_*$. Here, M_* and M_{s} are the stellar masses of the central and satellite candidate, respectively; r_{p} is the projected distance from the satellite candidate to its central; and Δv is the line-of-sight velocity difference between them. They found that the $M_{\text{h}}\text{-}\sigma_{\text{s}}$ relation so obtained has a power-law slope of about 3, but the amplitude of the relation is lower than that obtained from simulations (see Section 4.4).

We apply the same method to select satellite candidates for central galaxies. The centrals are divided into samples based on either their M_* , or σ_* , or M_{AM} (see Section 4.4). The distribution of the corresponding satellite candidates in the phase space (r_{p} versus Δv) are shown in Figure 1. Here we only present the results for galaxies with $11.2 \leq \log M_*/M_{\odot} < 11.65$ in A-series samples. The results for other galaxy samples/subsamples are similar. As one can see, there are cone-like structures in the phase space for ATotal, AC1, AC2 and AC3, as indicated by black contour lines, respectively. The PDFs of Δv are shown in the lower panels. The distributions for the four subsamples are very similar to a Gaussian distribution. The peaks corresponding to the cone-like structures are contributed predominantly by satellites, while the tails that are out-

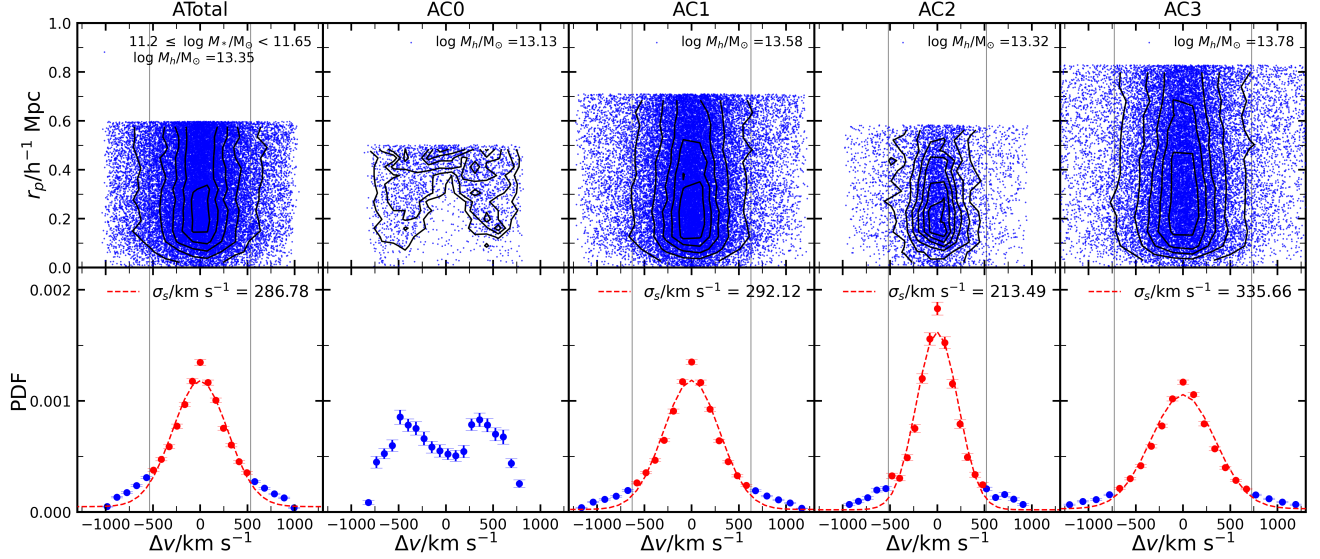


Figure 1. Upper panels: the data points and the contours show the distributions of satellite candidates in the projected phase space (r_p - Δv). Lower panels: the probability distributions of Δv (red and blue symbols) and the best-fitting curves for PDFs within $1.5v_{200m}$ (red symbols). The two gray vertical lines in each panel correspond to $\Delta v = \pm 1.5v_{200m}$. We only show the satellite candidates around centrals with $11.2 \leq \log M_*/M_\odot < 11.65$ in ATotal, AC0, AC1, AC2 and AC3 samples. The halo masses and satellite velocity dispersion of the samples are listed in the upper and lower panels, respectively. Please see Section 3.2 for details.

side of the cone are dominated by interlopers (Mamon et al. 2010). In contrast, AC0 galaxies has an empty cone-like structure and double-peaked Δv distribution. This is expected, because AC0 centrals have no satellite according to the group catalog, and the shown galaxies are mostly interlopers.

To eliminate interlopers as far as possible, we decide to only use satellite candidates with $|\Delta v| < |\Delta v|_{\text{cut}} = 1.5v_{200m}$ to estimate the satellite velocity dispersion. Our visual inspection shows that the cut at $1.5v_{200m}$ roughly corresponds to the boundary of the cone-like structures, as shown by the gray vertical lines in Figure 1. We performed a series of tests using a value of $|\Delta v|_{\text{cut}}$ ranging from 1.0 to $3.0v_{200m}$, and found that the results are stable as long as $|\Delta v|_{\text{cut}}$ is in the range of 1.3 - $1.8v_{200m}$. A smaller $|\Delta v|_{\text{cut}}$ excludes too many satellites in the cone-like structures and leads to poorer constraints. A larger $|\Delta v|_{\text{cut}}$, on the other hand, leads to a larger dispersion because of the inclusion of more interlopers. Please see Section 4.4 for more discussion.

The red symbols show the distributions of $|\Delta v|$ within $1.5v_{200m}$, with error bars estimated from 100 bootstrap samples. We fit the distributions to a functional form that is a Gaussian plus a constant,

$$P(\Delta v) = \frac{A}{\sqrt{2\pi}\sigma_v} e^{-\Delta v^2/2\sigma_v^2} + d. \quad (3)$$

The constant d is used to account for interlopers within the cone. We use the MCMC to fit the PDFs. The uncertainty of a SDSS galaxy redshift, which is about

35 km s^{-1} , results in an error of $\sigma_e = \sqrt{2} \times 35 = 49.5 \text{ km s}^{-1}$. We correct this and obtain the satellite velocity dispersion using

$$\sigma_s = \sqrt{\sigma_v^2 - \sigma_e^2}. \quad (4)$$

To compare with Zhang et al. (2022b), we use the same reference galaxy sample to select satellite candidates. This sample, selected from NYU-VAGC sample dr72 (Blanton et al. 2005), contains 510,605 galaxies, with r -band Petrosian apparent magnitude $r < 17.6$, r -band Petrosian absolute magnitude in the range of $-24 < M_{0.1r} < -16$, and the redshift in the range of $0.01 < z < 0.2$. Here, $M_{0.1r}$ is the r -band Petrosian absolute magnitude with $K + E$ corrected to the value at $z = 0.1$ (see Wang & Li 2019, for more details).

3.3. The combined halo mass proxies

In this section, we introduce our method for deriving new halo mass proxies by linearly combining two proxies presented above. Since we have no σ_s measurements for individual galaxies, we only use M_* , σ_* and M_{AM} to design new proxies. The three parameters have very different dynamical ranges, it is thus necessary to scale them before the combination. For a proxy D, we design a new parameter,

$$\text{Rank}_D = \frac{D - \min(D)}{\max(D) - \min(D)}, \quad (5)$$

where $\min(D)$ and $\max(D)$ represent the minimum and maximum values of the proxy, respectively. A new proxy

can then be designed by combining two proxies D and E as,

$$\text{Pr}(D, E, p) = (1 - p) * \text{Rank}_D + p * \text{Rank}_E, \quad (6)$$

where p is in the range of $0 \leq p \leq 1$. With $p = 0$, $\text{Pr}(D, E, p)$ is equivalent to the proxy D, while with $p = 1$, $\text{Pr}(D, E, p)$ is equivalent to the proxy E. Since M_{AM} is used, we use the B-series samples to examine the new proxies.

One way to evaluate the performance of a proxy is to check the dependence of the M_{h} -proxy scaling relation on other galaxy and group properties, such as N_{sat} and SFR. We choose to use the differences in the M_{h} -proxy scaling relations between BC0 and BC3 subsamples and between BSF and BQ subsamples to quantify the dependencies on N_{sat} and SFR, respectively. We first divide the BTotal sample into $N_{\text{b}} = 8$ equally-sized bins according to a new proxy, $\text{Pr}(D, E, p)$. Then we select galaxies that belong to BC0, BC3, BSF and BQ subsamples and derive their halo masses at each $\text{Pr}(D, E, p)$ bin based on weak lensing, respectively. We now have $M_{\text{h}}\text{-Pr}(D, E, p)$ relations for BC0, BC3, BSF and BQ subsamples. We use the following formula to calculate the difference between two scaling relations,

$$d_{\text{para}} = \frac{1}{N_{\text{b}}} \sum_{i=1}^{N_{\text{b}}} \frac{(\log M_{i,1} - \log M_{i,2})^2}{\text{err}_{i,1}^2 + \text{err}_{i,2}^2}, \quad (7)$$

where $\log M_{i,1}$, $\text{err}_{i,1}$, $\log M_{i,2}$ and $\text{err}_{i,2}$ are the halo masses and their uncertainties at the i th bin for the two scaling relations, respectively. Sometimes, the mean $\text{Pr}(D, E, p)$ at the largest or smallest $\text{Pr}(D, E, p)$ bin is very different between BC0 and BC3 (or between BSF and BQ). In order to compare the two scaling relations in a fair way, the halo mass and its uncertainty used in Equation 7 for BC3 and BSF are calculated using the linear interpolation method. To evaluate the uncertainty of d_{para} , we use the Monte Carlo method to generate $\log M_{i,1}$ and $\log M_{i,2}$ for each $\text{Pr}(D, E, p)$ bin, which follow Gaussian distributions with a mean equal to the weak lensing mass and a dispersion equal to the uncertainty. These new parameters can be used to calculate a new d_{para} . This procedure is repeated 500 times and we take the dispersion of the 500 d_{para} as the uncertainty. In the following, we use d_{SFR} and $d_{N_{\text{sat}}}$ to represent the dependencies of the scaling relation on SFR and N_{sat} , respectively (Section 4.5).

4. HALO MASS - PROXY SCALING RELATIONS

4.1. Stellar mass-halo mass scaling relation

We divide galaxies from the ATotal sample with $M_* \geq 10^{8.5} M_{\odot}$ into 8 M_* bins, equally spaced in the logarithm

of M_* with a bin size of 0.45 dex. Then, we use methods presented in Section 3 to obtain the ESD and derive the halo mass for each M_* bin. The ESD profiles and their best-fittings of four selected M_* bins are presented in Figure 2. The resulting SHMR is shown in Figure 3 as black solid diamonds. For comparison, we also show the SHMRs from the literature obtained using various methods, including galaxy groups, abundance matching, conditional luminosity function, weak lensing, and empirical models (e.g. Yang et al. 2009; Moster et al. 2010; Leauthaud et al. 2012; Kravtsov et al. 2018; Behroozi et al. 2019). The SHMR for ATotal is well consistent with these results.

Many parameters are correlated with M_{h} and M_* . These correlations may reflect possible dependencies of the SHMR on these parameters. We first consider N_{sat} . As shown in Section 2.1, the ATotal sample can be split into AC0, AC2 and AC3 subsamples according to N_{sat} . The ESDs and their best fitting profiles for these subsamples in four stellar mass bins are presented in Figure 2. At a given M_* , the amplitude of the ESD signal increases with increasing group richness. A direct comparison of the SHMRs can be found in the left panel of Figure 3, where only mass bins with more than 50 galaxies are presented. At the high mass end, the AC0 galaxies have a SHMR that tends to be slightly lower than that of ATotal, and AC3 galaxies tend to have the highest SHMR. We do not show the result for AC1 sample because AC1 is the sum of AC2 and AC3.

At given M_* , the halo mass is positively correlated with group richness (Johnston et al. 2007; Andreon et al. 2008; Viola et al. 2015) and the difference in M_{h} among samples is quite large. For the four most massive M_* bins, the differences in M_{h} between AC0 and AC3 are in the range of 0.5-0.8 dex. The SDSS galaxy sample is a magnitude limited sample. Some groups in AC0 sample may have large intrinsic N_{sat} , but their satellites are not detected due to the Malmquist bias. Such an effect dilutes the dependence on group richness. Therefore, the intrinsic dependence should be stronger than what we find here.

We then study the dependence of SHMR on SFR. The SHMR for star-forming (ASF) and quenched (AQ) galaxies are shown in the middle panel of Figure 3. Overall, star-forming galaxies reside in halos with a mean halo mass much lower than quenched ones of the same M_* , consistent with previous studies (e.g. More et al. 2011; Rodríguez-Puebla et al. 2015; Mandelbaum et al. 2016; Behroozi et al. 2019; Bilicki et al. 2021; Zhang et al. 2021, 2022b). The quenched galaxies in the second lowest mass bin have a much higher halo mass compared to the star-forming ones. One possible reason is that a

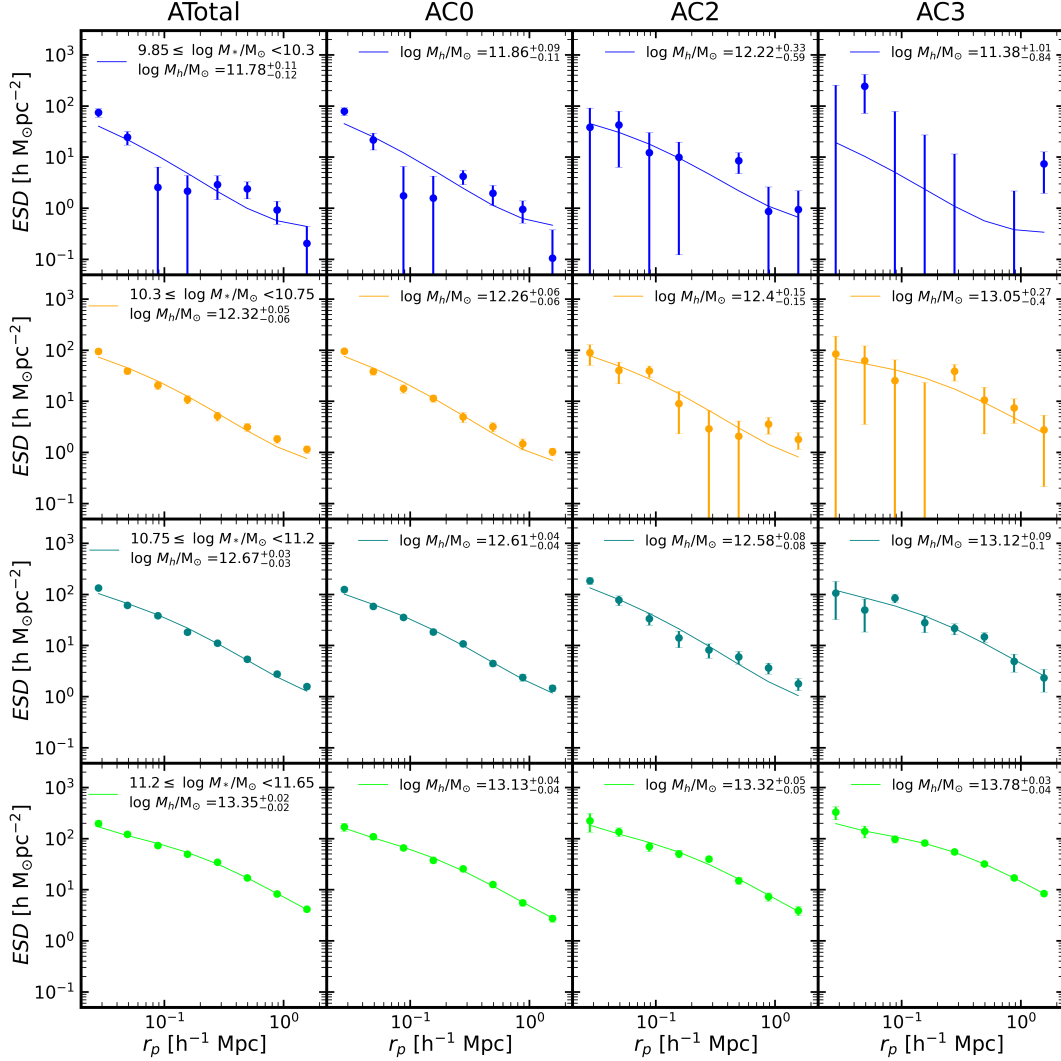


Figure 2. Excess surface density (ESD) profiles and the best fitting results. Different rows correspond to different M_* bins, and different columns correspond to different galaxy samples, including ATotal, AC0, AC1, AC2 and AC3. The error bars correspond to the standard deviation of 150 bootstrap samples. The best-fitting M_h are also presented.

significant fraction of galaxies in this mass bin are satellites, which are misidentified as centrals by group finder. Because satellites usually reside in more massive halos than centrals of the same mass, the misidentification can lead to overestimation of halo mass. We examined their ESD profile and found a bump-like structure from 0.1-1 Mpc/h, which is similar to the lensing signal produced by satellite galaxies (Yang et al. 2006; Li et al. 2014). Another possibility is that some of these galaxies reside in the splashback halos (Wang et al. 2023b). Since splashback halos have ever entered massive halos, they are close to massive halos and thus have similar bump on their ESD. Moreover, these galaxies are subject to a variety of environmental effects and thus very likely to be quenched.

To investigate the dependence of SHMR on σ_* , we divide the ATotal sample in each stellar mass bin into

small and large σ_* subsamples by the median σ_* of each M_* bin. Their SHMRs are shown in the right panel of Figure 3. We can see that the SHMR has the strongest dependence on σ_* in the middle stellar mass range. This dependence weakens towards the lower and higher stellar mass end. We will come back to the correlations among M_h , M_* and σ_* in the next subsection.

4.2. Halo mass-galaxy central stellar velocity dispersion scaling relation

In this subsection, we use the galaxy stellar velocity dispersion (σ_*) as a halo mass proxy and investigate the M_h - σ_* scaling relation. The ATotal sample is divided into 8 σ_* bins. The bin size varies with σ_* to ensure that each bin has reliable M_h measurement as much as possible. The M_h - σ_* relation for the ATotal sample is shown in Figure 4 as black solid diamonds. We can see

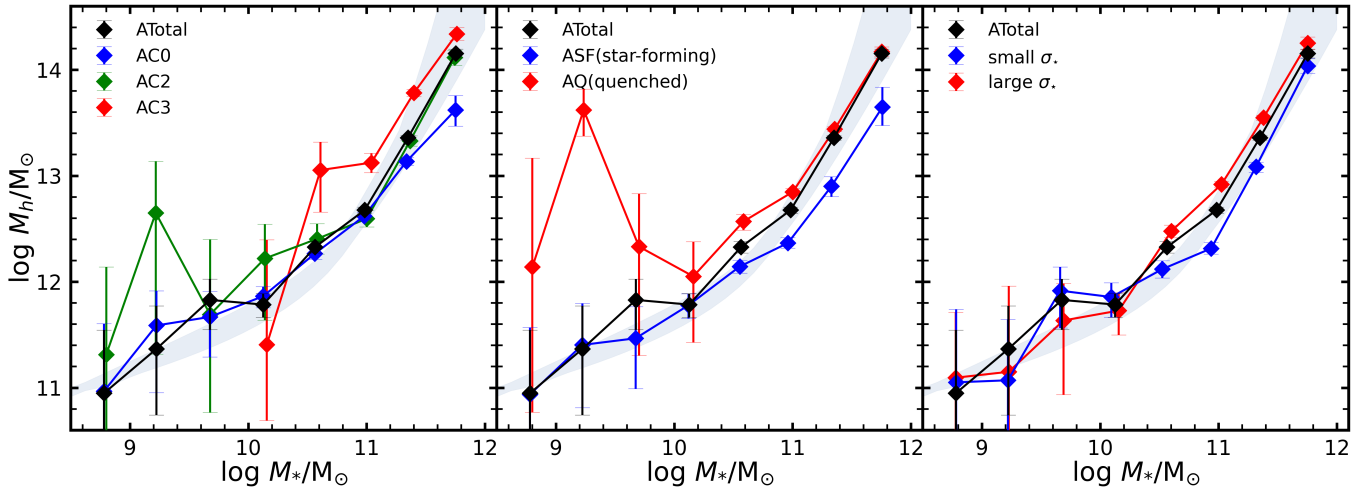


Figure 3. The dependence of SHMR on N_{sat} (left), SFR(middle) and σ_* (right). The black lines in the three panels show the SHMR for ATotal sample. The error bars reflect the 16% and 84% of the posterior distribution. The shaded region corresponds to the region covered by the SHMR curves published in Yang et al. (2009), Moster et al. (2010), Leauthaud et al. (2012), Kravtsov et al. (2018), and Behroozi et al. (2019).

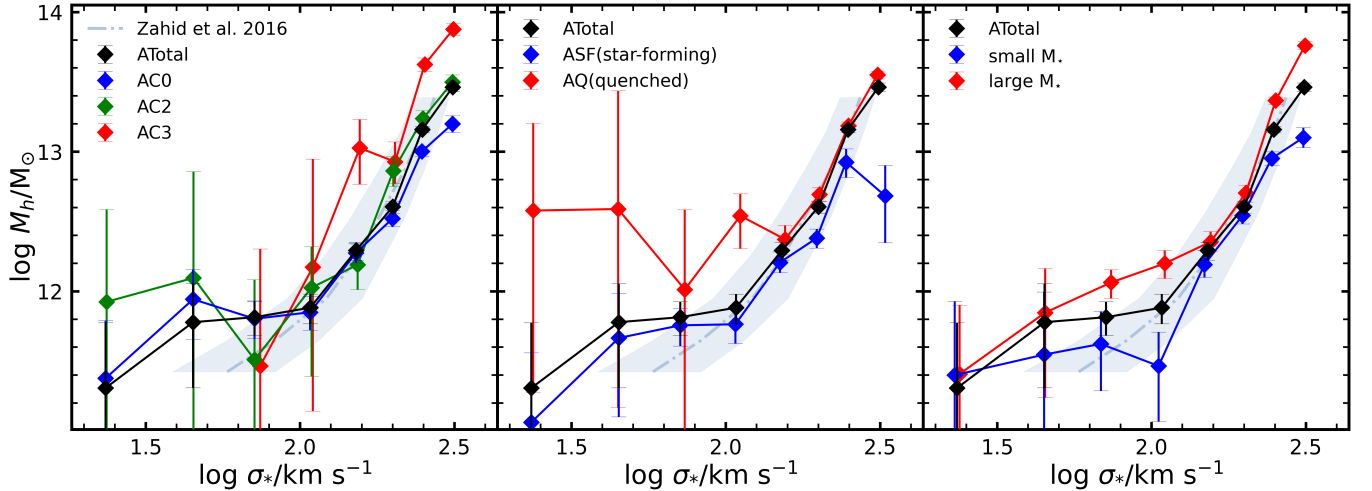


Figure 4. The dependence of the M_h - σ_* relation on N_{sat} (left), SFR(middle) and M_* (right). The black lines in the three panels show the M_h - σ_* relation for ATotal sample. The light-blue dot-dashed line and the shaded region show the relation from Zahid et al. (2016) and its scatter.

that galaxies with larger σ_* reside in more massive halos. For comparison, we also present the result of Zahid et al. (2016) who used the SHMR to assign the halo mass to each galaxy. Overall, our result is in good agreement with theirs.

We then examine the dependence of the M_h - σ_* relation on various parameters and only present the σ_* bins with galaxy number greater than 50. We first investigate the dependence on N_{sat} (left panel of Figure 4). Similar to the SHMR, the $M_h - \sigma_*$ relation strongly depends on N_{sat} . The uncertainties of halo masses at low σ_* bins are very large, no clear $M_h - N_{\text{sat}}$ correlation can be found in this regime. However, at the four largest σ_* bins where the halo masses are well constrained, M_h in-

creases significantly with N_{sat} at fixed σ_* . And the M_h difference between AC0 and AC3 is about 0.4-0.8 dex, similar to that for SHMR.

We now check the dependence of the M_h - σ_* relation on SFR(the middle panel of Figure 4). In the low σ_* range ($\log \sigma_* < 2.1$), because of the small number of quenched galaxies, the uncertainties in the halo masses of quenched galaxies are very large. In the middle σ_* range ($2.1 < \log \sigma_* < 2.4$), the halo mass difference at a given σ_* between star-forming and quenched galaxies is typically 0.2-0.3 dex, apparently smaller than the difference in the middle M_* range, typically 0.4-0.5 dex. This is not surprising, as σ_* is the most important factor for star formation quenching(see e.g. Bluck et al. 2020).

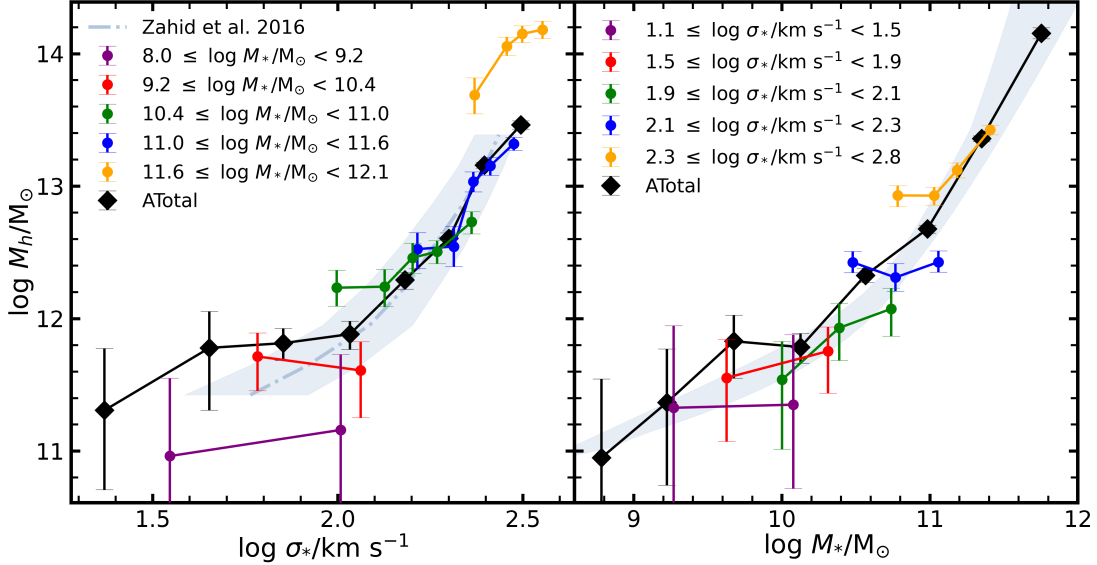


Figure 5. The dependence of M_h - σ_* relation on M_* (left panel) and M_h - M_* relation on σ_* (right panel). The black lines in the two panels show the results for ATotal sample. The color-coded lines in the left (right) panel show the results for M_* -controlled (σ_* -controlled) subsamples. Please see Section 4.2 for details. The dot-dashed line and the shaded region in the left panel are the same as those in Figure 4. And the shaded region in the right panel is the same as that in Figure 3.

For the results in the largest σ_* bin, the halo mass of the star-forming galaxies is significantly lower than that of the corresponding quenched galaxies. This result can be attributed to the fact that the star-forming galaxies contain a batch of galaxies with high star-forming efficiency (see Zhang et al. 2022b). At a given σ_* , the halo masses of star-forming and quenched galaxies are still significantly different. It suggests that other processes, likely related to halo mass, also play an important role in quenching star formation.

We then split each σ_* bin into two equally-sized subsamples according to their M_* . The results for these subsamples are presented in the right panel of Figure 4. The uncertainties in the two lowest σ_* bins are too large to allow quantifying the difference. For larger σ_* , the dependence of the M_h - σ_* relation on M_* is almost absent at $\log \sigma_* \sim 2.3$ and becomes stronger towards lower and higher σ_* . It is thus interesting to investigate the bivariate correlation in more detail. We perform two tests. In the first test, we investigate the M_h - σ_* relation at a given M_* . For galaxies in a given M_* bin, we split them into several (2 to 5, dependent on the weak lensing signal) equally-sized subsamples by σ_* . Our inspection shows that these subsamples with different σ_* are significantly different in the M_* distribution though they are selected within the same M_* bin. To eliminate the potential bias, we re-select galaxies from these σ_* subsamples so that they have similar M_* distributions (see Appendix for the method). The re-selected subsamples are referred to as the M_* -controlled subsamples. In the second test, we investigate the SHMR at a given

σ_* . Similar to the first test, we construct σ_* -controlled subsamples to eliminate the influence of σ_* .

The left panel of Figure 5 shows the M_h - σ_* relations for M_* -controlled subsamples. At $\log \sigma_* < 2.1$, M_h is almost independent of σ_* but strongly dependent on M_* . It suggests that for these galaxies, the observed M_h - σ_* relation is dominated by the M_h - M_* relation. At $2.1 < \log \sigma_* < 2.4$, we see a strong dependence of M_h on σ_* even when M_* is well controlled. Interestingly, galaxies in two different M_* bins (green and blue) follow almost the same trend, defined by the ATotal sample. It means that the SHMR in this range is driven by σ_* , totally opposite to the trend seen in low-mass galaxies. At $\log \sigma_* > 2.4$, we see the dependence on both M_* and σ_* .

Similar conclusions can also be drawn from the SHMR results for the σ_* -controlled subsamples, as shown in the right panel of Figure 5. In the lowest three σ_* bins, the SHMRs generally follow the same trend as that of the ATotal sample in the low stellar mass range ($\log M_*/M_\odot < 10.4$). It means that σ_* has a negligible impact on SHMR at the low M_* end. In the middle stellar mass range ($10.4 < \log M_*/M_\odot < 11.1$), the SHMRs in three σ_* bins ($1.9 < \log \sigma_* < 2.8$) deviate from each other and all have very flat slopes. It means that M_h is independent of M_* after controlling σ_* . Therefore, the SHMR in this mass range is mainly driven by the M_h - σ_* relation. In the massive stellar mass end ($\log M_*/M_\odot > 11.1$), the SHMR in the largest σ_* bin is almost consistent with the SHMR of ATotal sample. However, since there is only one σ_* bin at this mass

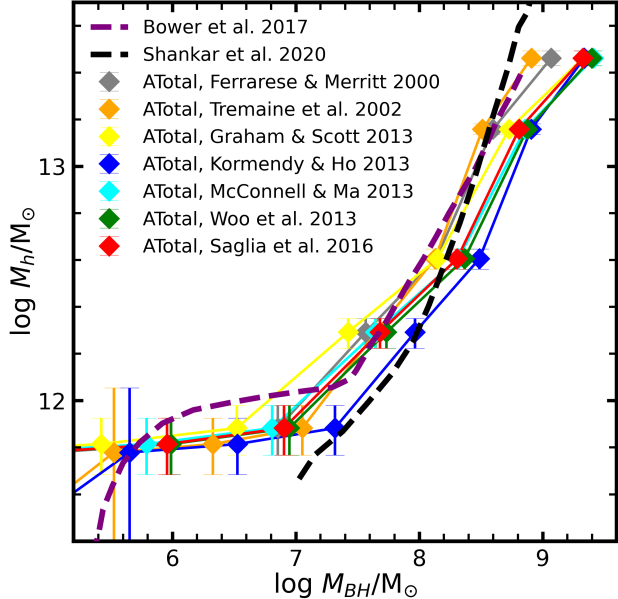


Figure 6. M_h - M_{BH} relations. We apply seven $M_{\text{BH}}-\sigma_*$ relations from the literature as indicated to convert the $M_h-\sigma_*$ relation into the M_h - M_{BH} relations. For comparison, we show the model result of Bower et al. (2017) in purple dashed line and the observational result of Shankar et al. (2020) in black dashed line.

range, we can not disentangle the correlations with σ_* and M_* . In general, these results are in good agreement with those from Figure 3 and 4.

One important application of the $M_h-\sigma_*$ relation is that it can be used to study the connection between dark matter halos and super-massive black holes in galaxy center, which are thought to play an essential role in galaxy evolution. It is well known that σ_* is tightly correlated with the black hole mass (M_{BH}). We can convert the $M_h-\sigma_*$ relation into M_h - M_{BH} relation using the $M_{\text{BH}}-\sigma_*$ relation. Here, we adopt seven $M_{\text{BH}}-\sigma_*$ relations (Ferrarese & Merritt 2000; Tremaine et al. 2002; Graham & Scott 2013; Kormendy & Ho 2013; McConnell & Ma 2013; Woo et al. 2013; Saglia et al. 2016), which are derived from different galaxy samples. The resultant M_h - M_{BH} relations are shown in Figure 6.

Though the uncertainty in the $M_{\text{BH}}-\sigma_*$ relation leads to a large uncertainty in the M_{BH} estimation, all of these results follow a general trend. When M_{BH} increases rapidly from $10^{5.0}$ to $10^{7.4}M_\odot$, M_h only increases about 0.2 dex, from $10^{11.8}$ to $10^{12.0}M_\odot$. It hints at a rapid growth of black holes as their host halos reach $\log M_h/M_\odot \sim 12.0$, consistent with that AGNs usually reside in halos of $\log M_h/M_\odot \sim 12.0$ (e.g. Zhang et al. 2021). At $\log M_h/M_\odot > 12.0$, when M_{BH} increases from $10^{7.4}$ to 10^9M_\odot , M_h increases from $10^{12.0}$ to $10^{13.4}M_\odot$, indicating a nearly linear correlation be-

tween M_{BH} and M_h . Our M_h - M_{BH} relation shows a transition in black hole growth at $\log M_h/M_\odot \sim 12.0$ and $\log M_{\text{BH}}/M_\odot \sim 7.4$.

It is possible that the independence of M_h on M_{BH} at low mass end is caused by the relatively large uncertainties of the low σ_* . Because large uncertainties can erase the intrinsic difference among galaxies in several low σ_* bins. To check this possibility, we investigate the errors of σ_* measurement, taken from NYU-VAGC, in the four lowest σ_* bins of the ATotal sample. Our tests show that the four lowest σ_* bins (at least the second to fourth bin) have significantly different intrinsic σ_* considering the errors. It is also supported by the fact that the M_* distributions in the four bins are significantly different. Another important factor is the uncertainty of $M_{\text{BH}}-\sigma_*$ relation at the low mass end. We adopt seven relations, which are obtained using different galaxy sample and have different slopes. Similar transition is seen in all results. It is expected because the transition originates from the $M_h-\sigma_*$ relation where the transition is clearly presented. We also calculate the $M_{\text{BH}}-M_h$ relation for early-type galaxies and find a similar transition. These tests indicate the uncertainties in σ_* measurement and $M_{\text{BH}}-\sigma_*$ relation do not significantly change our conclusion.

For comparison, we show the M_h - M_{BH} relation obtained by Shankar et al. (2020). Shankar et al. (2020) estimated M_h using the abundance matching technique and M_{BH} using the M_*-M_{BH} relation for quiescent galaxies (Saintonge et al. 2016). In general, our predictions are consistent with theirs, but lower at high mass and higher at low mass. Shankar et al. (2020) also provided a M_h - M_{BH} relation based on a so-called bias-corrected galaxy sample, which significantly deviates from ours. Because we adopt different methods to derive M_h and M_{BH} , it is difficult to determine the exact cause of this discrepancy. We also show the result of an analytic model developed by Bower et al. (2017). Their model prediction is in good agreement with our observational result at $\log M_{\text{BH}}/M_\odot > 6$. They suggested that when M_h is close to $10^{12}M_\odot$, star-formation feedback can not effectively drive outflow and black holes start to grow rapidly. When $M_h > 10^{12}M_\odot$, the ISM will eventually be consumed by star formation or expelled by AGN feedback, and the black hole growth rate is reduced. Bower et al. (2017) assumed that the further growth of black holes is limited by the binding energy within the cooling radius of their host halos, which leads to the linear relationship between the halo mass and the black hole mass at $\log M_h/M_\odot > 12$. Apparently, the $M_h-\sigma_*$ and M_h - M_{BH} relations contain valuable information about galaxy formation and evolution. We will

come back to this issue in the near future (Li. et al. in preparation).

4.3. Halo mass-abundance-matching mass scaling relation

In this subsection, we adopt the abundance matching halo mass (hereafter M_{AM}) based on group stellar mass as the halo mass proxy. The following tests are based on the B-series samples. We divide the BTotal sample into 8 M_{AM} bins, the sizes of which are varied to obtain reliable halo mass measurements as far as possible. The resultant M_h - M_{AM} relation is shown in Figure 7 as black solid diamonds. For comparison, we also present the M_h - M_{AM} relation from Luo et al. (2018), shown as the cyan circles. Our result is in excellent agreement with that of Luo et al. (2018). The M_h - M_{AM} relation is very close to a one-to-one relation. At $\log M_h/M_\odot > 12.5$, the weak lensing measured halo mass is slightly smaller than the abundance matching mass. At $\log M_h/M_\odot < 12.5$, M_h becomes slightly larger than M_{AM} .

We then examine the dependence of the M_h - M_{AM} relation on various parameters. The upper-left panel shows the dependence on group richness. Different from the SHMR and M_h - σ_* relation, the dependence of the M_h - M_{AM} relation on N_{sat} is much weaker. M_{AM} is estimated based on the sum of stellar masses of group member galaxies (see Yang et al. 2007, for the details). Therefore, the satellite information has already been involved in the estimation of M_{AM} . At low mass, the result for the BTotal is dominated by the BC0 galaxies, which have no satellite. It means that the M_h - M_{AM} relation is approximately equivalent to the M_h - M_* relation. It might explain the small change in the M_h - M_{AM} relation at $\log M_h/M_\odot \sim 12.5$. We also divide galaxies in each M_{AM} bin into two equally-sized subsamples according to their M_* . The M_h - M_{AM} relations for the small and large M_* galaxies are presented in the lower-left panel of Figure 7. As one can see, they both closely follow the overall M_h - M_{AM} relation and exhibit almost no difference. It means that the M_h - M_* relation can be fully explained by the M_h - M_{AM} relation. Therefore, M_{AM} is a more powerful proxy than M_* . It is not surprising because M_{AM} is estimated based on the group stellar mass, which also includes the contribution of central galaxies.

The M_h - M_{AM} relations for star-forming and quenched galaxies are shown in the upper-right panel of Figure 7. The halo masses for the quenched galaxies are apparently higher than the corresponding star-forming galaxies over all M_{AM} range in consideration. The halo mass differences are rather large, ranging from ~ 0.3 to 0.9 dex, comparable to the difference for the M_h - M_* rela-

tion and larger than that for the M_h - σ_* relation. The dependence of the M_h - M_{AM} relation on σ_* is also significant (lower-right panel). At low M_{AM} , the dependence on σ_* is weak. At middle M_{AM} , the dependence becomes very pronounced, with large σ_* galaxies residing in more massive halos than the corresponding small σ_* galaxies. At high M_{AM} , this dependence becomes weak, and almost disappears in the largest M_{AM} bin. Overall, M_{AM} is a better proxy than M_* and σ_* . However, the dependencies on SFR and σ_* suggest that the M_h - M_{AM} scaling relation is still sensitive to galaxy formation processes.

4.4. Halo mass-satellite velocity dispersion scaling relation

The halo mass-satellite velocity dispersion (σ_s) scaling relation has been widely studied in the literature (e.g. Rines & Diaferio 2006; Yang et al. 2007; Hoekstra 2007; Evrard et al. 2008; Munari et al. 2013; Rines et al. 2013; Saro et al. 2013; Ruel et al. 2014; Gonzalez et al. 2015; Han et al. 2015; Viola et al. 2015; Rines et al. 2016; Abdullah et al. 2020; Gonzalez et al. 2021; Rana et al. 2022). Most of these studies used the σ_s data measured for individual galaxy groups/clusters even though these groups have only a few member galaxies. We, however, adopt a stacking method to measure the average σ_s for a given galaxy sample (see the method description in Section 3.2). Our method needs a halo mass tracer to divide a galaxy sample into several bins. As shown in the above sections, M_* , σ_* and M_{AM} are all strongly correlated with halo mass. We thus decide to use these three quantities as halo mass tracers. When we use M_* and σ_* as tracers, the tests are performed on the A-series samples. When M_{AM} is considered, the tests are performed on the B-series samples. We divide the galaxy samples into 8 bins according to these tracers. Since both the weak lensing and satellite kinematics techniques are performed using the stacking method, the uncertainties are very large when the sample size is small. For clarity, we only present the results with galaxy number greater than 100.

We first show the results using M_* and σ_* as tracers in Figure 8. They are referred to as the M_* -tracer (solid crosses) and σ_* -tracer (solid diamonds) relations, respectively. For reference, we also present the scaling relations obtained from simulations (Evrard et al. 2008; Munari et al. 2013; Saro et al. 2013). The blue dashed line shows the relation from Evrard et al. (2008) that used dark matter particles to calculate the satellite velocity dispersion. They obtained a slope of 2.98, in good agreement with the virial scaling relation (a slope of 3). The red dashed line shows the result from a hydro-

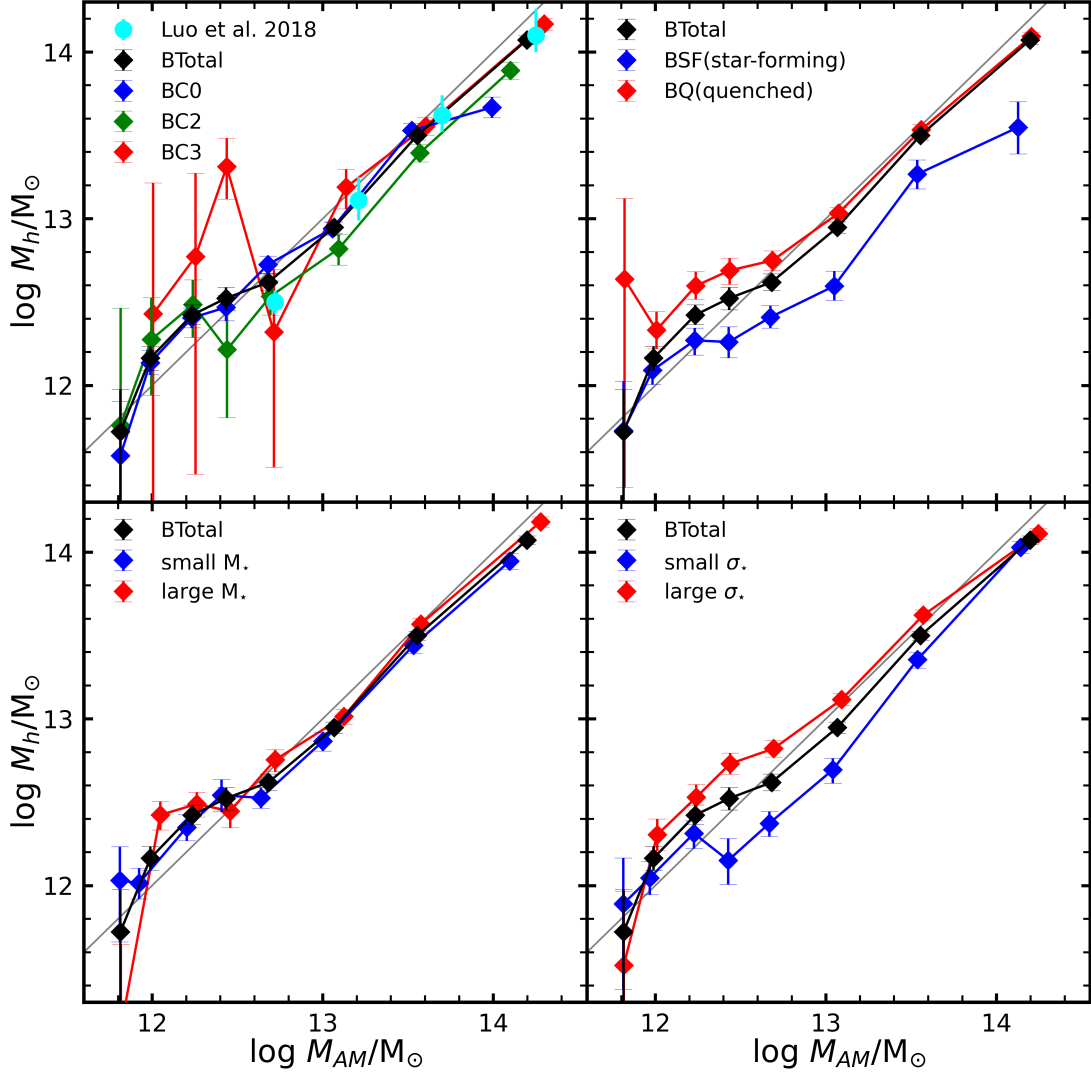


Figure 7. The dependence of the M_h - M_{AM} relation on N_{sat} (upper-left), SFR(upper-right), M_* (lower-left) and σ_* (lower-right). The cyan circles show the results from Luo et al. (2018), and the gray line in each panel shows the one-to-one relation.

dynamical simulation with star formation and AGN feedback(Munari et al. 2013), in which the simulated galaxies are used to calculate the dispersion. They got a slope of 2.75, slightly less than 3. The purple dashed line shows the relation from Saro et al. (2013), which has a slope of 2.91. They used galaxies yielded by a semi-analytic galaxy formation model and only considered galaxy clusters. The best-fitting parameters for the three results are listed in Table 2. Note that their halo masses have already been converted into our halo mass definition.

The results from Zhang et al. (2022b) are also presented in gray color, which used M_* as a tracer and adopted a larger Δv cut of $3v_{200\text{m}}$. They obtained a slope close to the simulations and an amplitude, however, much lower than the simulations (Table 2). Although σ_s in Zhang et al. (2022b) is overestimated, the

halo mass estimated using the M_h - σ_s relation is still reliable. Because the M_h - σ_s relation is calibrated by using weak lensing measured halo mass. The reasons for the large discrepancy between the M_h - σ_s relation of Zhang et al. (2022b) and the simulation relations are twofold: (1) the contamination of interlopers as discussed in Section 3.2; (2) the weighting bias discussed in van den Bosch et al. (2004). To check the first issue, we adopt a Δv cut of $1.5v_{200\text{m}}$ and present the results of ATotal sample in the left panel of Figure 8. As one can see, a small Δv cut can significantly reduce the contamination. However, the discrepancy is still severe. AC0 galaxies have no satellite and thus contribute little to the σ_s measurement, but they have on average lower M_h than AC1 galaxies and thus significantly lower the mean halo mass. It means that AC0 galaxies have different weighting factors in the measurements of M_h and σ_s .

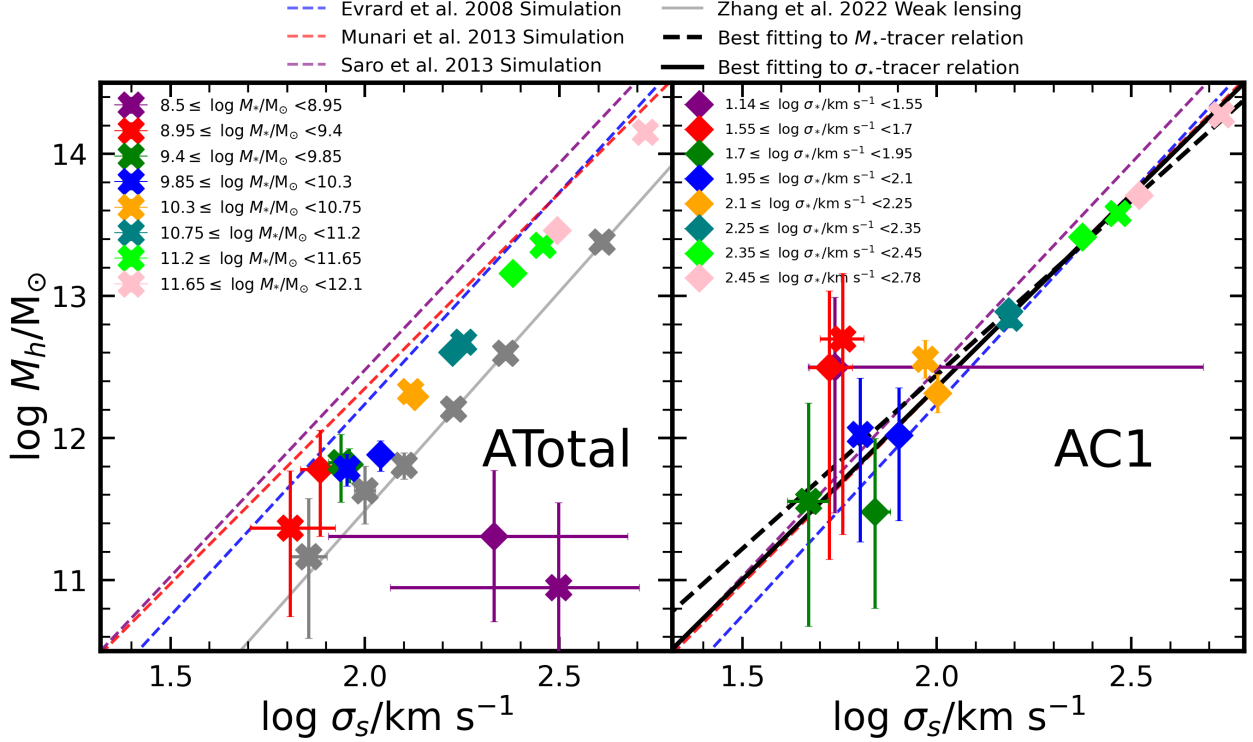


Figure 8. The M_h - σ_s relations using M_* (crosses) or σ_* (diamonds) as a tracer. Different colors represent different M_* or σ_* bins as labeled in the two panels. The left and right panels show the results based on Atotal and AC1 samples, respectively. The black dashed and solid lines are the best-fittings to M_* - and σ_* -tracer relations, respectively. The red, purple and blue dashed lines show the simulation results. The gray solid crosses are taken from Zhang et al. (2022b) and the gray line is its best-fitting (left panel). Please see Section 4.4 for the details.

Table 2. The fitting parameters for M_h - σ_s relation

Reference	$b^{(a)}$	$k^{(b)}$	Tracer ^(c)	Data ^(d)
Evrard et al. (2008)	6.28	2.98	–	simulation
Munari et al. (2013)	6.85	2.75	–	simulation
Saro et al. (2013)	6.66	2.91	–	simulation
Han et al. (2015)	$7.77^{+0.08}_{-0.08}$	$2.17^{+0.34}_{-0.34}$	σ_s	observation
Viola et al. (2015)	$9.07^{+0.06}_{-0.07}$	$1.89^{+0.27}_{-0.27}$	σ_s	observation
Rana et al. (2022)	$10.03^{+0.02}_{-0.02}$	$1.52^{+0.1}_{-0.1}$	σ_s	observation
Zhang et al. (2022b)	$5.33^{+0.11}_{-0.11}$	$3.08^{+0.05}_{-0.05}$	M_*	observation
Sample	$b^{(a)}$	$k^{(b)}$	Tracer ^(c)	Data ^(d)
AC1	$7.55^{+0.06}_{-0.06}$	$2.45^{+0.03}_{-0.03}$	M_*	observation
AC1	$6.94^{+0.09}_{-0.09}$	$2.71^{+0.04}_{-0.04}$	σ_*	observation
BC1	$7.31^{+0.06}_{-0.06}$	$2.57^{+0.02}_{-0.02}$	M_{AM}	observation
BC1, star-forming	$6.12^{+0.2}_{-0.22}$	$3.08^{+0.1}_{-0.09}$	M_{AM}	observation
BC1, quenched	$7.23^{+0.07}_{-0.07}$	$2.61^{+0.03}_{-0.03}$	M_{AM}	observation
BC2	$6.38^{+0.13}_{-0.14}$	$3.02^{+0.06}_{-0.06}$	M_{AM}	observation
BC3	$6.95^{+0.12}_{-0.12}$	$2.72^{+0.05}_{-0.05}$	M_{AM}	observation

(a) Zero-point(b) in Equation 8.

(b) Slope(k) in Equation 8.

(c) Samples are divided into subsamples according to the tracer for fitting.

(d) The origin of the data used for fitting.

To reduce the weighting bias, we exclude AC0 galaxies and apply our method to AC1 galaxies only. The new scaling relations lie very close to the simulation results, as shown in the right panel of Figure 8.

We use a power-law function to fit the data,

$$\log M_h/M_\odot = k \log \sigma_s/\text{km s}^{-1} + b. \quad (8)$$

The best-fitting slopes are 2.45 and 2.71 for the M_* -tracer and σ_* -tracer relations, respectively (see Table 2). The best-fitting results are also presented in black lines in Figure 8. We can see that the σ_* -tracer relation is perfectly consistent with the relation measured from hydrodynamical simulation (Munari et al. 2013). We also use M_{AM} as a tracer to divide BC1 sample into 8 M_{AM} bins. The obtained M_h - σ_s scaling relation and its fitting result are presented in Figure 9 and Table 2. The M_{AM} -tracer relation is also very similar to the simulation results. It is almost the same as the results of Evrard et al. (2008) and Munari et al. (2013) at the massive end and slightly higher than them at the low-mass end. The slope of the relation is 2.57 (Table 2), between those of the M_* - and σ_* -tracer relations. Our measurements are more similar to the result of hydrodynamical simulation. It might be a signal for velocity bias.

We then check the dependence of the M_h - σ_s relation on other galaxy and group properties. Here, we only present the M_{AM} -tracer results. The results for BC2 and BC3 samples are shown in Figure 9 and Table 2. The relations for the two populations are both similar to the simulation results. The relation for BC2 (close to the simulation result of Saro et al. (2013)) is slightly higher than that for BC3 (close to the result of Munari et al. (2013)) at high σ_s . We also split the BC1 sample into star-forming and quenched galaxies. The scaling relations for the two types of galaxies are also presented in Figure 9 and Table 2. In general, the two relations are very similar and both are close to the simulation results. And the slope for star-forming galaxies seems slightly steeper than that for quenched galaxies. Given the large uncertainties for star-forming galaxies at low mass, the difference is not significant.

In addition, we perform a test with a double-Gaussian model (see e.g. More et al. 2011) to repeat Figure 8 and Figure 9. In general, the obtained M_h - σ_s relations from the double-Gaussian model are in agreement with the simulation relations too. However, they are more noisy compared to the results shown in this paper. It is likely that one of the two Gaussian components sometimes fit the interlopers rather than the satellites, resulting in a larger error bar in σ_s . Therefore, we don't use the double-Gaussian model to analyze the satellite kinematics in this paper.

Finally, we compare our M_{AM} -tracer M_h - σ_s relations of BC1 sample with previous observational studies based on weak lensing in Figure 10. Hoekstra (2007) and Gonzalez et al. (2015) focused on individual galaxy clusters. In general, these clusters lie around the simulation relations with relatively large scatter. Han et al. (2015), Viola et al. (2015), Gonzalez et al. (2021), and Rana et al. (2022) calculated σ_s for individual groups with more than 3 to 5 galaxy members and then divided their group sample into subsamples according to σ_s . Therefore, they all used σ_s as a tracer. We list their best fitting parameters (if available) in Table 2. These researches usually got slopes (~ 2 or < 2) that are much flatter than the simulation slopes. Some of them got amplitudes lower than the simulations. Various possible interpretations for the discrepancies have been proposed, such as rich group selection bias, interlopers, velocity bias and non-equilibrium systems.

Different from these studies, we divide galaxies by their M_* , σ_* or M_{AM} rather than σ_s . After carefully dealing with interlopers and weighting bias, our M_h - σ_s relations are in good agreement with the simulation results in a broad halo mass range. In addition, the M_h - σ_s relation depends weakly on N_{sat} and SFR. All of these suggest that group richness, velocity bias and merging systems can not induce the large deviations presented in these papers. The estimation of σ_s for individual groups is sensitive to interlopers and the number of group members. The large uncertainty can smear and weaken the correlation between M_h and σ_s , as shown in previous studies.

4.5. The linearly combined proxies

The above analyses show that the M_* -, σ_* - and M_{AM} - M_h relations depends on N_{sat} and SFR in different manners. It is thus interesting to check whether the combination of these proxies can provide a better proxy (see Han et al. 2015, for a relevant study). In Section 3.3, we introduce our method for generating a new proxy. We construct three sets of new proxies, $\text{Pr}(M_*, M_{\text{AM}}, p)$, $\text{Pr}(\sigma_*, M_{\text{AM}}, p)$, and $\text{Pr}(M_*, \sigma_*, p)$. To check the performance of the new proxy, we defined two parameters, $d_{N_{\text{sat}}}$ and d_{SFR} (Equation 7), to quantify the dependencies of the M_h -Pr relation on N_{sat} and SFR, respectively. A larger $d_{N_{\text{sat}}}$ or d_{SFR} means a stronger dependence on N_{sat} or SFR, and thus a worse proxy. When the parameters are equal to one, it means that the difference is mainly dominated by the uncertainties. Note that our tests are all performed with the B-series samples.

We first examine the combination of M_* and M_{AM} . Figure 11 show $d_{N_{\text{sat}}}$ and d_{SFR} as functions of p . We can see that $d_{N_{\text{sat}}}$ quickly decreases with increasing p

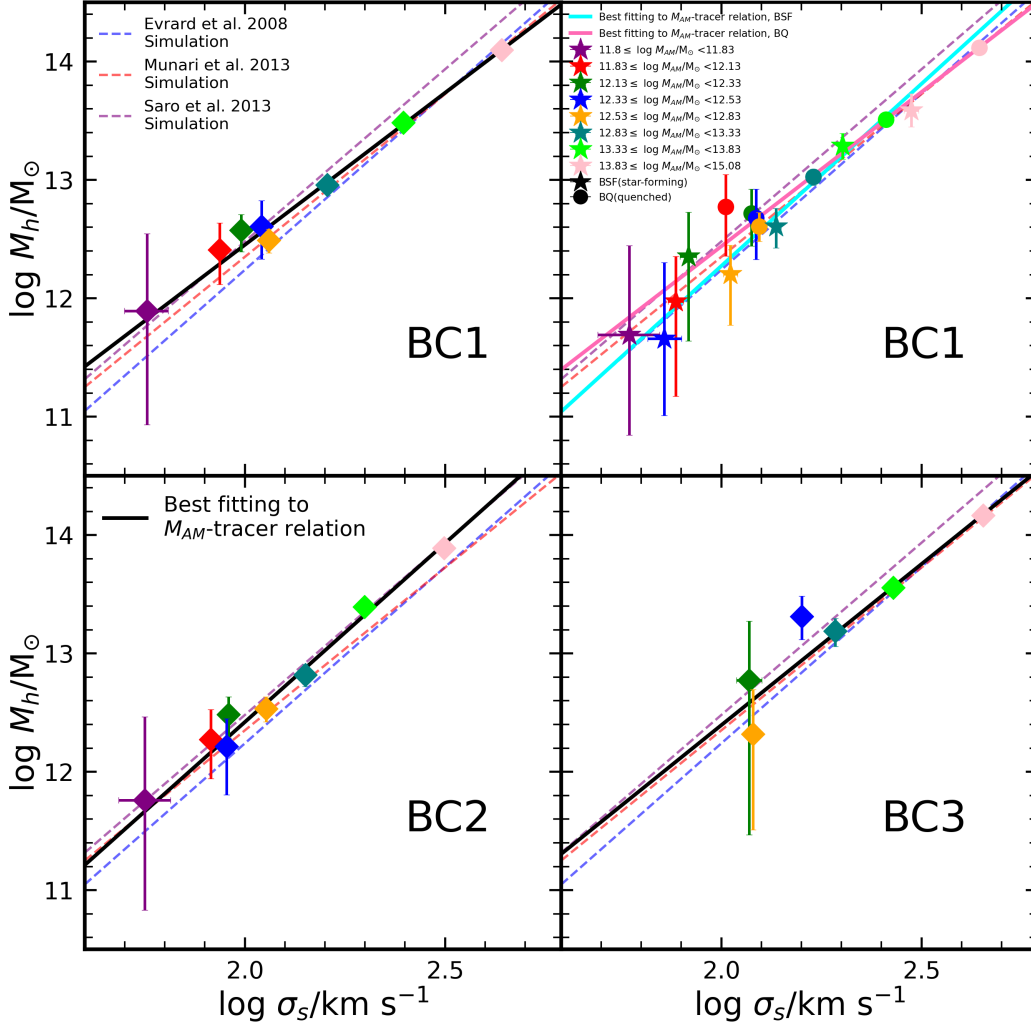


Figure 9. The M_h - σ_s relations using M_{AM} as a tracer. Different colors represent different M_{AM} bins as labeled in the upper-right panel. The upper-left, lower-left and lower-right panels show the results of BC1, BC2 and BC3, respectively. The upper-right panel shows the results for star-forming (solid stars) and quenched (solid circles) galaxies in BC1 sample. In each panel, the solid line is the best-fitting to the corresponding sample, and the red, purple and blue dashed lines are the relations from simulations.

at $p < 0.3$ and then remains unchanged at $d_{N_{\text{sat}}} \sim 3$. It means that the M_h - M_{AM} relation is less dependent on N_{sat} than the SHMR, well consistent with the above results. The parameter d_{SFR} is around 10 and slightly decreases with increasing p . It is also consistent with the results shown above that M_{AM} - and M_* - M_h relations depend on SFR in a similar manner. We thus conclude that M_{AM} is a better proxy than M_* and that the combination of the two parameters can not improve the performance.

We then examine the combination of σ_* and M_* . The results are presented in the right panel of Figure 11. As one can see, $d_{N_{\text{sat}}}$ is very large, about 25, and almost independent of p . It means that both σ_* - and M_* - M_h relations are strongly dependent on N_{sat} , consistent with the results shown in Figure 3 and Figure 4. d_{SFR} gradually decreases with increasing p . It is con-

sistent with that the M_h - σ_* relation is less sensitive to SFR than the SHMR. These tests suggest that σ_* is, on average, a better proxy than M_* . However, it does not mean that σ_* is a better proxy of halo mass than M_* over any mass range. For example, we find that M_* is better than σ_* for low mass halos (Section 4.2). Note that d_{SFR} measures the SFR dependence averaged over a large halo mass range weighted with halo mass uncertainties. Since the M_h uncertainties for low mass halos are much larger than those for massive halos, the contribution of low mass halos to d_{SFR} is negligible.

Finally, we examine the combination of σ_* and M_{AM} (the middle panel of Figure 11). $d_{N_{\text{sat}}}$ decreases quickly with increasing p at $p < 0.3$, then almost remains unchanged around unity at $0.3 < p < 0.9$, and increases at $p > 0.9$. While d_{SFR} is almost constant at $p < 0.3$ and then gradually increases with increasing p . Therefore,

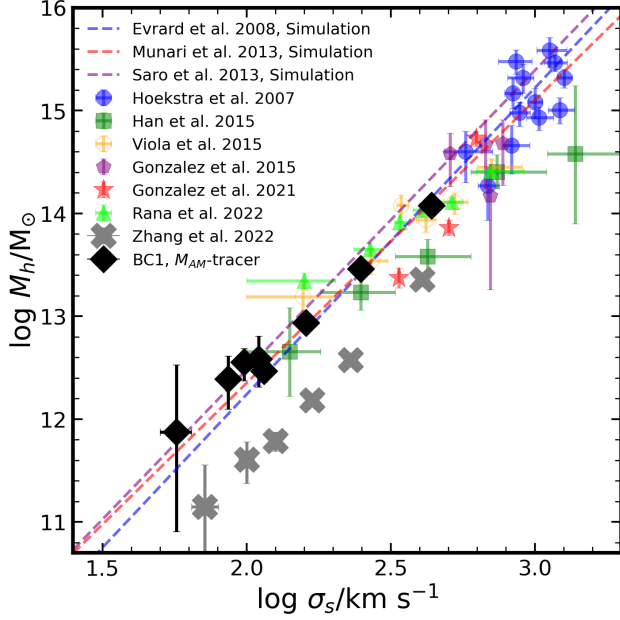


Figure 10. The M_h - σ_s relations from simulations and observations. As indicated in the figure, the color-coded dashed lines are the simulation results and the color-coded and gray symbols are the results from the literature with weak lensing measured M_h . For comparison, we also show our results for BC1 sample with M_{AM} as the halo mass tracer in black solid diamonds.

both $d_{N_{\text{sat}}}$ and d_{SFR} reach the minimum around $p = 0.3$. In fact, the combined proxy $\text{Pr}(\sigma_*, M_{AM}, 0.3)$ has almost the smallest $d_{N_{\text{sat}}}$ and d_{SFR} among the three sets of combined proxies. It means that the obtained M_h - $\text{Pr}(\sigma_*, M_{AM}, 0.3)$ relation would have the smallest scatter among all the proxies that we have explored in this section.

As mentioned above, the two parameters $d_{N_{\text{sat}}}$ and d_{SFR} are dominated by massive halos that have M_h measurements with high signal-to-noise ratio. They are thus unable to reflect the performance of the proxy at different mass bins, particularly at low mass. Future imaging surveys, such as Legacy Survey of Space and Time⁴, the Chinese Space Station Optical Survey (Gong et al. 2019) and the Wide Field Survey Telescope (WFST Collaboration et al. 2023) can provide much better data which allows us to explore the performance of different proxies in details.

5. SUMMARY AND DISCUSSION

In this paper, we use the DECaLS shear catalog to constrain the halo masses (M_h) of SDSS central galaxies and investigate the scaling relations between M_h

and four single halo mass proxies, including stellar mass (M_*), central stellar velocity dispersion (σ_*), group stellar mass ranked abundance matching halo mass (M_{AM}) and satellite kinematics (σ_s). We also examine the dependence of these scaling relations on galaxy internal properties, including M_* , σ_* and specific star formation rate (sSFR), and external properties, including group richness (N_{sat}). These dependencies can be used to examine the performance of these halo mass proxies and understand the galaxy formation processes. We also construct a series of new halo mass proxies by linearly combining two proxies and quantify their performances. In the following, we summarize our results and briefly discuss the implications.

Overall, we find that halo mass is strongly correlated with M_* , σ_* , M_{AM} and σ_s . Galaxies with larger M_* , σ_* , M_{AM} and σ_s tend to live in more massive halos. The four obtained scaling relations are in good agreement with previous observation or simulation results.

The M_h - M_* and M_h - σ_* scaling relations are strongly dependent on N_{sat} . At a given M_* or σ_* , the halo mass increases with N_{sat} . The halo mass difference between galaxies with $N_{\text{sat}} = 0$ and $N_{\text{sat}} \geq 3$ can reach about 0.7 dex at high M_* or σ_* ends. We suggest that the intrinsic dependence should be even stronger because our galaxy sample is magnitude limited. The halo abundance matching (HAM) technique that uses central galaxy properties as indicators of halo mass may fail to recover the halo masses of groups with large N_{sat} . Since these groups have a large number of satellites, such a failure may cause a bias on the predicted two-point correlation function at a small scale. Our results further suggest that the galaxy clusters selected based on N_{sat} may be biased to high M_*/M_h clusters.

The M_h - M_* and M_h - σ_* relations are also dependent on the SFR of central galaxies. It means a higher baryon-to-star conversion efficiency ($M_*/M_h / (\Omega_b / \Omega_m)$) for star-forming galaxies than for quiescent galaxies. It may place an important constraint on AGN feedback, which is thought to suppress the conversion efficiency. We convert the M_h - σ_* relation into the M_h - M_{BH} relation. At $\log M_h / M_\odot < 12.0$ or $\log M_{\text{BH}} / M_\odot < 7.4$, M_{BH} is weakly correlated with M_h . It hints at a rapid black hole growth. At $\log M_h / M_\odot > 12.0$ or $\log M_{\text{BH}} / M_\odot > 7.4$, M_{BH} linearly correlates with M_h . It indicates a transition of black hole growth. More studies are required to understand the underlying processes.

We investigate the correlations among M_h , M_* and σ_* . At small M_* or σ_* (roughly $\log M_*/M_\odot < 10.4$ or $\log \sigma_* < 2.1$), M_* is more closely related to M_h than σ_* ; In the intermediate M_* or σ_* range (roughly $10.4 < \log M_*/M_\odot < 11.1$ or $2.1 < \log \sigma_* < 2.4$), σ_*

⁴ <https://www.lsst.org/>

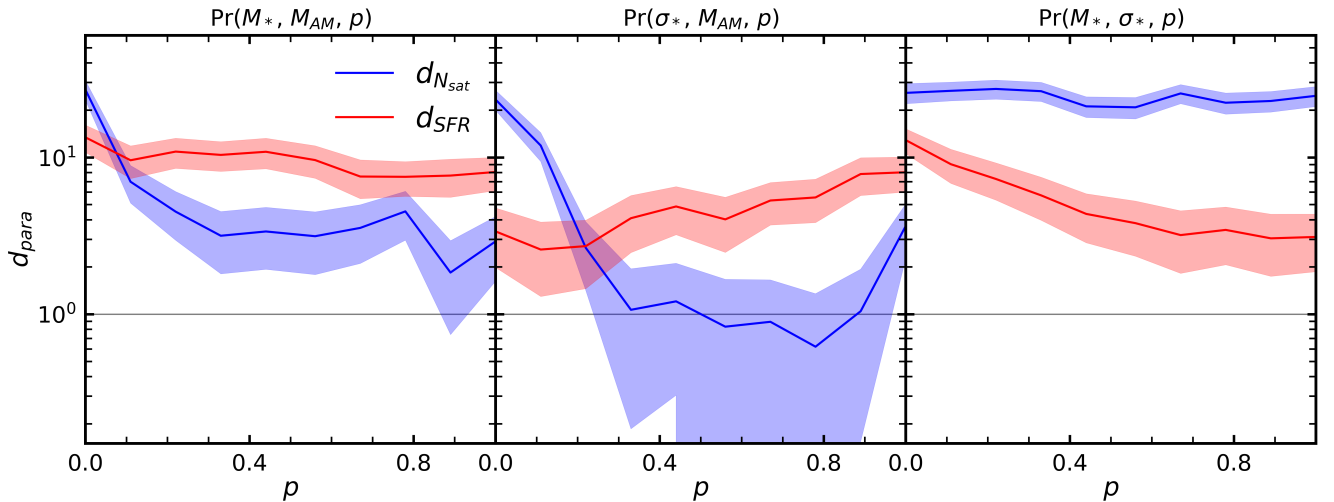


Figure 11. The performance of the combined proxy, measured with d_{para} (Equation 7), as a function of p . The left, middle and right panels show the results for the combination between M_* - M_{AM} , σ_* - M_{AM} and M_* - σ_* , respectively. In each panel, the blue and red lines correspond to the results for $d_{N_{\text{sat}}}$ and d_{SFR} , respectively. The corresponding blue and red shaded regions are the 1σ scatter (see Section 3.3 for the detail). The gray horizontal line shows $d_{\text{para}}=1$.

is more closely related with M_{h} than M_* ; At large M_* or σ_* (roughly $\log M_*/M_{\odot} > 11.1$ or $\log \sigma_* > 2.4$), M_{h} correlates with both parameters. The bivariate correlation suggests a complex connection among the growth of galaxy stellar mass, galaxy structure, black hole mass, and halo mass. It implies different growth patterns for galaxies at different stages. Higher quality weak lensing data are required to reexamine this issue.

Another examined halo mass proxy is M_{AM} . Our results show that the $M_{\text{h}}-M_{\text{AM}}$ relation is close to the one-to-one relation. Different from the SHMR and $M_{\text{h}}-\sigma_*$ relations, the $M_{\text{h}}-M_{\text{AM}}$ relation is weakly dependent on N_{sat} and independent of the stellar mass of central galaxies. It is expected because the estimation of M_{AM} is based on the mass of total member galaxies, so M_{AM} has already included the contribution of satellites and centrals. However, the $M_{\text{h}}-M_{\text{AM}}$ relation shows a strong dependence on SFR and σ_* . It hints that galaxy formation processes still have an important impact on the relationship. Overall, M_{AM} is a better halo mass proxy than M_* and σ_* .

The fourth scaling relation we investigate is the $M_{\text{h}}-\sigma_{\text{s}}$ relation. We use M_* , σ_* and M_{AM} as the halo mass tracers to divide a galaxy sample into subsamples and obtain the mean σ_{s} and M_{h} for each subsample using stacking method. After carefully handling the interloper contamination and weighting bias, we obtain $M_{\text{h}}-\sigma_{\text{s}}$ relations in good agreement with the simulation results, in particular the hydrodynamical simulation, from $\log M_{\text{h}}/M_{\odot} < 12.0$ to $\log M_{\text{h}}/M_{\odot} > 14.0$. Moreover, the scaling relation shows weak dependence on N_{sat} and SFR. Therefore, σ_{s} is the best proxy of halo mass among all these single proxies in consideration. It is expected

because the scaling relation originates from virialized systems and is insensitive to galaxy formation processes. However, the estimation of σ_{s} for individual groups is a serious challenge because of the interlopers and small satellite numbers.

Finally, we construct new halo mass proxies by linearly combining two single proxies. We examine three sets of combinations, including M_* - M_{AM} , σ_* - M_{AM} and M_* - σ_* combinations. We use the dependencies of the halo mass-new proxy scaling relation on N_{sat} and SFR to check the performance of the new proxy. The combination of σ_* and M_{AM} is better than the other two. It is because that the $M_{\text{h}}-M_{\text{AM}}$ scaling relation is insensitive to N_{sat} and the $M_{\text{h}}-\sigma_*$ scaling relation depends weakly on SFR. When M_{AM} contributes 30% and σ_* contributes 70% to the new proxy, the dependencies on N_{sat} and SFR are almost the weakest. We emphasize that our study provides a way to construct a halo mass proxy for individual groups and evaluate its performance. Future image surveys can provide much better lensing signals, which may allow us to study these proxies in detail and construct better ones.

ACKNOWLEDGEMENTS

We thank the referee and statistics editor for their useful reports. We thank Kai Wang from Peking University for his valuable suggestions on drawing. This work is supported by CAS Project for Young Scientists in Basic Research, Grant No. YSBR-062, the National Key R&D Program of China (grant Nos. 2018YFA0404503 and 2018YFA0404504), the National Natural Science Foundation of China (Nos. 12192224, 11733004, 11890693, 11890691, and 12073017), and the Fundamental Re-

search Funds for the Central Universities. We acknowledge the science research grants from the China Manned Space Project with Nos. CMS-CSST-2021-A01 and

CMS-CSST-2021-A03. The authors gratefully acknowledge the support of Cyrus Chun Ying Tang Foundations. The work is also supported by the Supercomputer Center of University of Science and Technology of China.

REFERENCES

- Abazajian, K. N., Adelman-McCarthy, J. K., Agüeros, M. A., et al. 2009, *ApJS*, 182, 543
- Abdullah, M. H., Wilson, G., Klypin, A., et al. 2020, *ApJS*, 246, 2, doi: [10.3847/1538-4365/ab536e](https://doi.org/10.3847/1538-4365/ab536e)
- Andreon, S., de Propris, R., Puddu, E., Giordano, L., & Quintana, H. 2008, *MNRAS*, 383, 102, doi: [10.1111/j.1365-2966.2007.12541.x](https://doi.org/10.1111/j.1365-2966.2007.12541.x)
- Barrow, J. D., Bhavsar, S. P., & Sonoda, D. H. 1984, *MNRAS*, 210, 19P
- Behroozi, P., Wechsler, R. H., Hearin, A. P., & Conroy, C. 2019, *MNRAS*, 488, 3143, doi: [10.1093/mnras/stz1182](https://doi.org/10.1093/mnras/stz1182)
- Bilicki, M., Dvornik, A., Hoekstra, H., et al. 2021, *A&A*, 653, A82, doi: [10.1051/0004-6361/202140352](https://doi.org/10.1051/0004-6361/202140352)
- Blanton, M. R., Schlegel, D. J., Strauss, M. A., et al. 2005, *AJ*, 129, 2562
- Bluck, A. F. L., Maiolino, R., Sánchez, S. F., et al. 2020, *MNRAS*, 492, 96, doi: [10.1093/mnras/stz3264](https://doi.org/10.1093/mnras/stz3264)
- Bluck, A. F. L., Mendel, J. T., Ellison, S. L., et al. 2016, *MNRAS*, 462, 2559
- Bocquet, S., Saro, A., Mohr, J. J., et al. 2015, *ApJ*, 799, 214, doi: [10.1088/0004-637X/799/2/214](https://doi.org/10.1088/0004-637X/799/2/214)
- Bower, R. G., Schaye, J., Frenk, C. S., et al. 2017, *MNRAS*, 465, 32, doi: [10.1093/mnras/stw2735](https://doi.org/10.1093/mnras/stw2735)
- Brinchmann, J., Charlot, S., White, S. D. M., et al. 2004, *MNRAS*, 351, 1151
- Caldwell, C. E., McCarthy, I. G., Baldry, I. K., et al. 2016, *MNRAS*, 462, 4117, doi: [10.1093/mnras/stw1892](https://doi.org/10.1093/mnras/stw1892)
- Carlberg, R. G., Yee, H. K. C., Morris, S. L., et al. 2001, *ApJ*, 552, 427, doi: [10.1086/320555](https://doi.org/10.1086/320555)
- Chen, Y., Mo, H. J., Li, C., & Wang, K. 2021a, *MNRAS*, 504, 4865, doi: [10.1093/mnras/stab695](https://doi.org/10.1093/mnras/stab695)
- Chen, Y., Mo, H. J., Li, C., et al. 2021b, *MNRAS*, 507, 2510, doi: [10.1093/mnras/stab2377](https://doi.org/10.1093/mnras/stab2377)
- Cole, S., Lacey, C. G., Baugh, C. M., & Frenk, C. S. 2000, *MNRAS*, 319, 168, doi: [10.1046/j.1365-8711.2000.03879.x](https://doi.org/10.1046/j.1365-8711.2000.03879.x)
- Conroy, C., Prada, F., Newman, J. A., et al. 2007, *ApJ*, 654, 153, doi: [10.1086/509632](https://doi.org/10.1086/509632)
- Croton, D. J., Springel, V., White, S. D. M., et al. 2006, *MNRAS*, 365, 11
- Cui, W., Davé, R., Peacock, J. A., Anglés-Alcázar, D., & Yang, X. 2021, *Nature Astronomy*, 5, 1069, doi: [10.1038/s41550-021-01404-1](https://doi.org/10.1038/s41550-021-01404-1)
- Dekel, A., & Silk, J. 1986, *ApJ*, 303, 39, doi: [10.1086/164050](https://doi.org/10.1086/164050)
- Dey, A., Schlegel, D. J., Lang, D., et al. 2019, *AJ*, 157, 168, doi: [10.3847/1538-3881/ab089d](https://doi.org/10.3847/1538-3881/ab089d)
- Diemer, B. 2018, *ApJS*, 239, 35, doi: [10.3847/1538-4365/aace8c](https://doi.org/10.3847/1538-4365/aace8c)
- Evrard, A. E., Bialek, J., Busha, M., et al. 2008, *ApJ*, 672, 122, doi: [10.1086/521616](https://doi.org/10.1086/521616)
- Fabian, A. C. 2012, *ARA&A*, 50, 455
- Fall, S. M., & Efstathiou, G. 1980, *MNRAS*, 193, 189, doi: [10.1093/mnras/193.2.189](https://doi.org/10.1093/mnras/193.2.189)
- Ferrarese, L., & Merritt, D. 2000, *ApJL*, 539, L9, doi: [10.1086/312838](https://doi.org/10.1086/312838)
- Foreman-Mackey, D., Hogg, D. W., Lang, D., & Goodman, J. 2013, *PASP*, 125, 306, doi: [10.1086/670067](https://doi.org/10.1086/670067)
- Gong, Y., Liu, X., Cao, Y., et al. 2019, *ApJ*, 883, 203, doi: [10.3847/1538-4357/ab391e](https://doi.org/10.3847/1538-4357/ab391e)
- Gonzalez, E. J., Foëx, G., Nilo Castellón, J. L., et al. 2015, *MNRAS*, 452, 2225, doi: [10.1093/mnras/stv787](https://doi.org/10.1093/mnras/stv787)
- Gonzalez, E. J., Rodriguez, F., Merchán, M., et al. 2021, *MNRAS*, 504, 4093, doi: [10.1093/mnras/stab1168](https://doi.org/10.1093/mnras/stab1168)
- Graham, A. W., & Scott, N. 2013, *ApJ*, 764, 151, doi: [10.1088/0004-637X/764/2/151](https://doi.org/10.1088/0004-637X/764/2/151)
- Han, J., Eke, V. R., Frenk, C. S., et al. 2015, *MNRAS*, 446, 1356, doi: [10.1093/mnras/stu2178](https://doi.org/10.1093/mnras/stu2178)
- Heckman, T. M., & Best, P. N. 2014, *ARA&A*, 52, 589, doi: [10.1146/annurev-astro-081913-035722](https://doi.org/10.1146/annurev-astro-081913-035722)
- Hoekstra, H. 2007, *MNRAS*, 379, 317, doi: [10.1111/j.1365-2966.2007.11951.x](https://doi.org/10.1111/j.1365-2966.2007.11951.x)
- Hopkins, P. F., Quataert, E., & Murray, N. 2012, *MNRAS*, 421, 3522, doi: [10.1111/j.1365-2966.2012.20593.x](https://doi.org/10.1111/j.1365-2966.2012.20593.x)
- Hudson, M. J., Gillis, B. R., Coupon, J., et al. 2015, *MNRAS*, 447, 298, doi: [10.1093/mnras/stu2367](https://doi.org/10.1093/mnras/stu2367)
- Johnston, D. E., Sheldon, E. S., Wechsler, R. H., et al. 2007, arXiv e-prints, arXiv:0709.1159. <https://arxiv.org/abs/0709.1159>
- Kauffmann, G., & Charlot, S. 1998, *MNRAS*, 294, 705, doi: [10.1046/j.1365-8711.1998.01322.x](https://doi.org/10.1046/j.1365-8711.1998.01322.x)
- Kauffmann, G., Heckman, T. M., Tremonti, C., et al. 2003, *MNRAS*, 346, 1055, doi: [10.1111/j.1365-2966.2003.07154.x](https://doi.org/10.1111/j.1365-2966.2003.07154.x)
- Kormendy, J., & Ho, L. C. 2013, *ARA&A*, 51, 511, doi: [10.1146/annurev-astro-082708-101811](https://doi.org/10.1146/annurev-astro-082708-101811)

- Kravtsov, A. V., Vikhlinin, A. A., & Meshcheryakov, A. V. 2018, *Astronomy Letters*, 44, 8, doi: [10.1134/S1063773717120015](https://doi.org/10.1134/S1063773717120015)
- Lange, J. U., van den Bosch, F. C., Zentner, A. R., Wang, K., & Villarreal, A. S. 2019a, *MNRAS*, 487, 3112, doi: [10.1093/mnras/stz1466](https://doi.org/10.1093/mnras/stz1466)
- . 2019b, *MNRAS*, 482, 4824, doi: [10.1093/mnras/sty2950](https://doi.org/10.1093/mnras/sty2950)
- Leauthaud, A., Finoguenov, A., Kneib, J.-P., et al. 2010, *ApJ*, 709, 97, doi: [10.1088/0004-637X/709/1/97](https://doi.org/10.1088/0004-637X/709/1/97)
- Leauthaud, A., Tinker, J., Bundy, K., et al. 2012, *ApJ*, 744, 159, doi: [10.1088/0004-637X/744/2/159](https://doi.org/10.1088/0004-637X/744/2/159)
- Li, C., Jing, Y. P., Mao, S., et al. 2012, *ApJ*, 758, 50, doi: [10.1088/0004-637X/758/1/50](https://doi.org/10.1088/0004-637X/758/1/50)
- Li, C., Wang, L., & Jing, Y. P. 2013, *ApJL*, 762, L7, doi: [10.1088/2041-8205/762/1/L7](https://doi.org/10.1088/2041-8205/762/1/L7)
- Li, R., Shan, H., Mo, H., et al. 2014, *MNRAS*, 438, 2864, doi: [10.1093/mnras/stt2395](https://doi.org/10.1093/mnras/stt2395)
- Lu, Y., Yang, X., Shi, F., et al. 2016, *ApJ*, 832, 39, doi: [10.3847/0004-637X/832/1/39](https://doi.org/10.3847/0004-637X/832/1/39)
- Luo, W., Yang, X., Lu, T., et al. 2018, *ApJ*, 862, 4, doi: [10.3847/1538-4357/aacaf1](https://doi.org/10.3847/1538-4357/aacaf1)
- Mamon, G. A., Biviano, A., & Murante, G. 2010, *A&A*, 520, A30, doi: [10.1051/0004-6361/200913948](https://doi.org/10.1051/0004-6361/200913948)
- Mandelbaum, R., Seljak, U., & Hirata, C. M. 2008, *JCAP*, 2008, 006, doi: [10.1088/1475-7516/2008/08/006](https://doi.org/10.1088/1475-7516/2008/08/006)
- Mandelbaum, R., Seljak, U., Kauffmann, G., Hirata, C. M., & Brinkmann, J. 2006, *MNRAS*, 368, 715, doi: [10.1111/j.1365-2966.2006.10156.x](https://doi.org/10.1111/j.1365-2966.2006.10156.x)
- Mandelbaum, R., Wang, W., Zu, Y., et al. 2016, *MNRAS*, 457, 3200, doi: [10.1093/mnras/stw188](https://doi.org/10.1093/mnras/stw188)
- McConnell, N. J., & Ma, C.-P. 2013, *ApJ*, 764, 184, doi: [10.1088/0004-637X/764/2/184](https://doi.org/10.1088/0004-637X/764/2/184)
- McKay, T. A., Sheldon, E. S., Johnston, D., et al. 2002, *ApJL*, 571, L85, doi: [10.1086/341364](https://doi.org/10.1086/341364)
- Mo, H., van den Bosch, F. C., & White, S. 2010, *Galaxy Formation and Evolution*
- Mo, H. J., & White, S. D. M. 1996, *MNRAS*, 282, 347, doi: [10.1093/mnras/282.2.347](https://doi.org/10.1093/mnras/282.2.347)
- More, S., van den Bosch, F. C., Cacciato, M., et al. 2011, *MNRAS*, 410, 210, doi: [10.1111/j.1365-2966.2010.17436.x](https://doi.org/10.1111/j.1365-2966.2010.17436.x)
- Moster, B. P., Somerville, R. S., Maulbetsch, C., et al. 2010, *ApJ*, 710, 903, doi: [10.1088/0004-637X/710/2/903](https://doi.org/10.1088/0004-637X/710/2/903)
- Munari, E., Biviano, A., Borgani, S., Murante, G., & Fabjan, D. 2013, *MNRAS*, 430, 2638, doi: [10.1093/mnras/stt049](https://doi.org/10.1093/mnras/stt049)
- Navarro, J. F., Frenk, C. S., & White, S. D. M. 1997, *ApJ*, 490, 493, doi: [10.1086/304888](https://doi.org/10.1086/304888)
- Planck Collaboration, Ade, P. A. R., Aghanim, N., et al. 2016, *A&A*, 594, A13, doi: [10.1051/0004-6361/201525830](https://doi.org/10.1051/0004-6361/201525830)
- Posti, L., & Fall, S. M. 2021, *A&A*, 649, A119, doi: [10.1051/0004-6361/202040256](https://doi.org/10.1051/0004-6361/202040256)
- Posti, L., Fraternali, F., & Marasco, A. 2019, *A&A*, 626, A56, doi: [10.1051/0004-6361/201935553](https://doi.org/10.1051/0004-6361/201935553)
- Rana, D., More, S., Miyatake, H., et al. 2022, *MNRAS*, 510, 5408, doi: [10.1093/mnras/stac007](https://doi.org/10.1093/mnras/stac007)
- Rines, K., & Diaferio, A. 2006, *AJ*, 132, 1275, doi: [10.1086/506017](https://doi.org/10.1086/506017)
- Rines, K., Geller, M. J., Diaferio, A., & Kurtz, M. J. 2013, *ApJ*, 767, 15, doi: [10.1088/0004-637X/767/1/15](https://doi.org/10.1088/0004-637X/767/1/15)
- Rines, K. J., Geller, M. J., Diaferio, A., & Hwang, H. S. 2016, *ApJ*, 819, 63, doi: [10.3847/0004-637X/819/1/63](https://doi.org/10.3847/0004-637X/819/1/63)
- Rodríguez-Puebla, A., Avila-Reese, V., Yang, X., et al. 2015, *ApJ*, 799, 130, doi: [10.1088/0004-637X/799/2/130](https://doi.org/10.1088/0004-637X/799/2/130)
- Romeo, A. B., Agertz, O., & Renaud, F. 2020, *MNRAS*, 499, 5656, doi: [10.1093/mnras/staa3245](https://doi.org/10.1093/mnras/staa3245)
- Ruel, J., Bazin, G., Bayliss, M., et al. 2014, *ApJ*, 792, 45, doi: [10.1088/0004-637X/792/1/45](https://doi.org/10.1088/0004-637X/792/1/45)
- Saglia, R. P., Opitsch, M., Erwin, P., et al. 2016, *ApJ*, 818, 47, doi: [10.3847/0004-637X/818/1/47](https://doi.org/10.3847/0004-637X/818/1/47)
- Saintonge, A., Catinella, B., Cortese, L., et al. 2016, *MNRAS*, 462, 1749, doi: [10.1093/mnras/stw1715](https://doi.org/10.1093/mnras/stw1715)
- Saro, A., Mohr, J. J., Bazin, G., & Dolag, K. 2013, *ApJ*, 772, 47, doi: [10.1088/0004-637X/772/1/47](https://doi.org/10.1088/0004-637X/772/1/47)
- Seo, G., Sohn, J., & Lee, M. G. 2020, *ApJ*, 903, 130, doi: [10.3847/1538-4357/abbd92](https://doi.org/10.3847/1538-4357/abbd92)
- Shankar, F., Allevato, V., Bernardi, M., et al. 2020, *Nature Astronomy*, 4, 282, doi: [10.1038/s41550-019-0949-y](https://doi.org/10.1038/s41550-019-0949-y)
- Silk, J., & Rees, M. J. 1998, *A&A*, 331, L1, <https://arxiv.org/abs/astro-ph/9801013>
- Sohn, J., Geller, M. J., Diaferio, A., & Rines, K. J. 2020, *ApJ*, 891, 129, doi: [10.3847/1538-4357/ab6e6a](https://doi.org/10.3847/1538-4357/ab6e6a)
- Tinker, J. L., Robertson, B. E., Kravtsov, A. V., et al. 2010, *ApJ*, 724, 878, doi: [10.1088/0004-637X/724/2/878](https://doi.org/10.1088/0004-637X/724/2/878)
- Tremaine, S., Gebhardt, K., Bender, R., et al. 2002, *ApJ*, 574, 740, doi: [10.1086/341002](https://doi.org/10.1086/341002)
- van den Bosch, F. C., Norberg, P., Mo, H. J., & Yang, X. 2004, *MNRAS*, 352, 1302, doi: [10.1111/j.1365-2966.2004.08021.x](https://doi.org/10.1111/j.1365-2966.2004.08021.x)
- Velander, M., van Uitert, E., Hoekstra, H., et al. 2014, *MNRAS*, 437, 2111, doi: [10.1093/mnras/stt2013](https://doi.org/10.1093/mnras/stt2013)
- Viola, M., Cacciato, M., Brouwer, M., et al. 2015, *MNRAS*, 452, 3529, doi: [10.1093/mnras/stv1447](https://doi.org/10.1093/mnras/stv1447)
- Wang, H., Zhang, J., Li, H., & Shen, Z. 2021, *ApJ*, 911, 10, doi: [10.3847/1538-4357/abe856](https://doi.org/10.3847/1538-4357/abe856)
- Wang, J., Yang, X., Zhang, J., et al. 2022, *ApJ*, 936, 161, doi: [10.3847/1538-4357/ac8986](https://doi.org/10.3847/1538-4357/ac8986)
- Wang, K., Chen, Y., Li, Q., & Yang, X. 2023a, *MNRAS*, 522, 3188, doi: [10.1093/mnras/stad1175](https://doi.org/10.1093/mnras/stad1175)

- Wang, K., Peng, Y., & Chen, Y. 2023b, MNRAS, 523, 1268, doi: [10.1093/mnras/stad1169](https://doi.org/10.1093/mnras/stad1169)
- Wang, L., & Li, C. 2019, MNRAS, 483, 1452, doi: [10.1093/mnras/sty3204](https://doi.org/10.1093/mnras/sty3204)
- Wechsler, R. H., & Tinker, J. L. 2018, ARA&A, 56, 435, doi: [10.1146/annurev-astro-081817-051756](https://doi.org/10.1146/annurev-astro-081817-051756)
- WFST Collaboration, Wang, T., Liu, G., et al. 2023, arXiv e-prints, arXiv:2306.07590, doi: [10.48550/arXiv.2306.07590](https://doi.org/10.48550/arXiv.2306.07590)
- White, S. D. M., & Rees, M. J. 1978, MNRAS, 183, 341, doi: [10.1093/mnras/183.3.341](https://doi.org/10.1093/mnras/183.3.341)
- Wojtak, R., & Mamon, G. A. 2013, MNRAS, 428, 2407, doi: [10.1093/mnras/sts203](https://doi.org/10.1093/mnras/sts203)
- Woo, J.-H., Schulze, A., Park, D., et al. 2013, ApJ, 772, 49, doi: [10.1088/0004-637X/772/1/49](https://doi.org/10.1088/0004-637X/772/1/49)
- Xu, K., & Jing, Y. 2022, ApJ, 926, 130, doi: [10.3847/1538-4357/ac4707](https://doi.org/10.3847/1538-4357/ac4707)
- Yang, X., Mo, H. J., & van den Bosch, F. C. 2003, MNRAS, 339, 1057, doi: [10.1046/j.1365-8711.2003.06254.x](https://doi.org/10.1046/j.1365-8711.2003.06254.x)
- . 2009, ApJ, 695, 900, doi: [10.1088/0004-637X/695/2/900](https://doi.org/10.1088/0004-637X/695/2/900)
- Yang, X., Mo, H. J., van den Bosch, F. C., & Jing, Y. P. 2005, MNRAS, 356, 1293
- Yang, X., Mo, H. J., van den Bosch, F. C., et al. 2006, MNRAS, 373, 1159, doi: [10.1111/j.1365-2966.2006.11091.x](https://doi.org/10.1111/j.1365-2966.2006.11091.x)
- . 2007, ApJ, 671, 153
- Zahid, H. J., Geller, M. J., Fabricant, D. G., & Hwang, H. S. 2016, ApJ, 832, 203, doi: [10.3847/0004-637X/832/2/203](https://doi.org/10.3847/0004-637X/832/2/203)
- Zahid, H. J., Sohn, J., & Geller, M. J. 2018, ApJ, 859, 96, doi: [10.3847/1538-4357/aabe31](https://doi.org/10.3847/1538-4357/aabe31)
- Zhang, J., Liu, C., Vaquero, P. A., et al. 2022a, AJ, 164, 128, doi: [10.3847/1538-3881/ac84d8](https://doi.org/10.3847/1538-3881/ac84d8)
- Zhang, J., Luo, W., & Foucaud, S. 2015, JCAP, 2015, 024, doi: [10.1088/1475-7516/2015/01/024](https://doi.org/10.1088/1475-7516/2015/01/024)
- Zhang, J., Zhang, P., & Luo, W. 2017, ApJ, 834, 8, doi: [10.3847/1538-4357/834/1/8](https://doi.org/10.3847/1538-4357/834/1/8)
- Zhang, J., Dong, F., Li, H., et al. 2019, The Astrophysical Journal, 875, 48, doi: [10.3847/1538-4357/ab1080](https://doi.org/10.3847/1538-4357/ab1080)
- Zhang, Z., Wang, H., Luo, W., et al. 2022b, A&A, 663, A85, doi: [10.1051/0004-6361/202142866](https://doi.org/10.1051/0004-6361/202142866)
- . 2021, A&A, 650, A155, doi: [10.1051/0004-6361/202040150](https://doi.org/10.1051/0004-6361/202040150)
- Zhou, R., Newman, J. A., Mao, Y.-Y., et al. 2021, MNRAS, 501, 3309, doi: [10.1093/mnras/staa3764](https://doi.org/10.1093/mnras/staa3764)
- Zhou, Y., & Han, J. 2022, ApJ, 939, 10, doi: [10.3847/1538-4357/ac9478](https://doi.org/10.3847/1538-4357/ac9478)
- Zou, H., Gao, J., Zhou, X., & Kong, X. 2019, The Astrophysical Journal Supplement Series, 242, 8, doi: [10.3847/1538-4365/ab1847](https://doi.org/10.3847/1538-4365/ab1847)

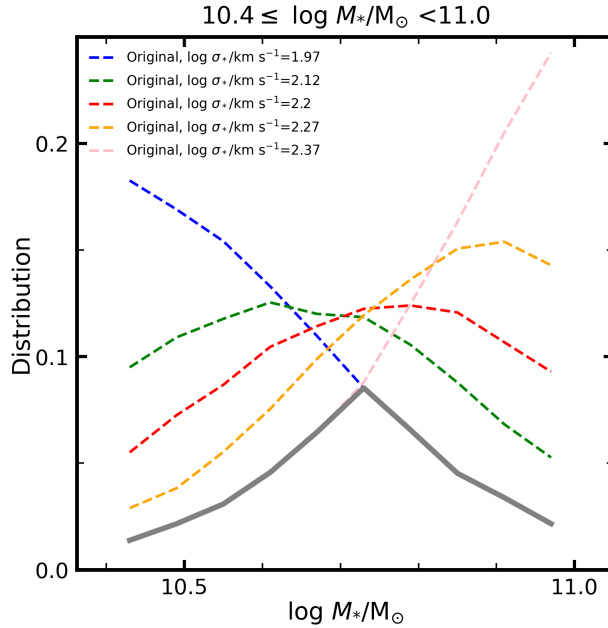


Figure 12. Stellar mass distributions of different galaxy samples in the same stellar mass bin. The color-coded dashed lines show the original M_* distributions for galaxies in different σ_* bins. These galaxies are restricted in the stellar mass range of $10.4 \leq \log M_*/M_\odot < 11$. The thick gray line shows the lower envelope of the dashed lines. Our controlled subsamples are selected in each σ_* bin according to the gray line.

APPENDIX

A. THE CONSTRUCTION OF CONTROLLED SAMPLES

Our purpose is to investigate the dependence of M_h on the parameter X with parameter Y controlled. We divide a galaxy sample within a Y range into several bins according to X . Galaxies in these different X bins have different distributions of Y parameter, although they are selected in the same Y range. To ensure that the dependence of M_h on X is not affected by the Y parameter, it is necessary to construct the Y -controlled subsamples.

Take the M_* -controlled subsamples in Section 4.2 as an example. We want to study the correlation between M_h and σ_* (X parameter) at a given M_* (Y parameter). We thus divide a galaxy sample in a given M_* range into several σ_* bins. Figure 12 shows the M_* probability distributions for galaxies of $10.4 \leq \log M_*/M_\odot < 11.0$ in five different σ_* bins (dashed lines). We can see that the M_* distributions are still very different, even in the relatively narrow M_* range. It is unsurprising because M_* and σ_* are strongly correlated. To construct M_* -controlled subsamples to eliminate the impact of M_* , we select galaxies in each σ_* bin following the distribution indicated by the thick gray line, which is the lower envelope of these dashed lines. This method ensures sufficient galaxies in every σ_* bin.